Complex interactions between precipitation, grain growth and recrystallization in a severely deformed Al-Zn-Mg-Cu alloy and consequences on the mechanical behavior

Amandine Duchaussoy, Xavier Sauvage, Alexis Deschamps, Frederic de Geuser, Gilles Renou, Zenji Horita

Complex interactions between precipitation, grain growth and recrystallization in a severely deformed Al-Zn-Mg-Cu alloy and consequences on the mechanical behavior

Amandine Duchaussoy[1,2,*], Xavier Sauvage[1], Alexis Deschamps[3], Frederic De Geuser[3], Gilles Renou[3], Zenji Horita[4,5]

[1] *Normandie Univ, UNIROUEN, INSA Rouen, CNRS, Groupe de Physique des Matériaux, 76000 Rouen, France*

[2] *Institute of Mechanics, Materials and Civil Engineering (iMMC-IMAP), Université catholique de Louvain, 1348, Louvain-La-Neuve, Belgium*

[3] *Univ. Grenoble Alpes, CNRS, Grenoble INP, SIMaP, F-38000 Grenoble, France*

[4] *WPI, International Institute for Carbon-Neutral Energy Research (I2CNER), Kyushu University, Fukuoka 819-0395, Japan*

[5] *Department of Materials Science and Engineering, Faculty of Engineering, Kyushu University, Fukuoka 819-0395, Japan*

**Correspondence: duchaussoy.amandine@laposte.net*

Materialia 15 (2021) 101028

https://doi.org/10.1016/j.mtla.2021.101028

Abstract:
Combining submicrometer grain size with nanoscaled precipitation is an attractive approach to achieve high yield stress with reasonable ductility in aluminum alloys. The control of super saturated solid solutions decomposition in ultrafine grain structure during precipitation annealing treatments is however a huge challenge. It raises indeed the general question of competition between precipitation, grain growth and recrystallization. All these microstructure changes are driven by the minimization of the free energy of the system but connected to three different factors, the thermodynamic driving force, the grain boundary energy and the dislocation density respectively. In this work, we have systematically investigated the interconnection of these mechanisms in an Al-Zn-Mg-Cu alloy processed by high pressure torsion at room temperature to achieve a submicrometer grain size from the solutionized state. Ageing heat treatments were carried out to study the precipitation kinetics using complementary characterization techniques such as in-situ small-angle X-ray scattering, differential scanning calorimetry, transmission electron microscopy and atom probe tomography. Experimental data clearly demonstrate that precipitation starts at much lower temperature in the deformed state and that the precipitation sequence is modified as compared to the classical coarse grain alloy. Beyond the detailed understanding of precipitation mechanisms and the competition with recrystallization and recovery processes, the systematic relationship between microstructural features and the mechanical behavior was also studied. A special emphasis was given on the specific contribution of precipitates nucleated heterogeneously along grain boundaries.

1. Introduction

The design of light weight structures for the aircraft and aerospace industries have fostered the design of new aluminum alloys during the past decades. Since plasticity in aluminum is triggered by the motion of dislocations, high mechanical strength can be achieved only through the design of alloys with an optimized distribution of obstacles to these crystalline defects. Strain hardening and solid solution hardening are the simplest approaches, but the strongest alloys require a fine distribution of nanoscaled precipitates, as in alloys from the 7xxx series. It is also well documented that reducing the grain size is an attractive strategy to further increase the yield stress (Hall and Petch law [1,2]). Since it has been demonstrated that ultrafine grain (UFG) structures can be achieved using severe plastic deformation (SPD), the combination of grain boundary (GB) strengthening and precipitate hardening has attracted a significant interest [3–26]. 7xxx series Al-Zn-Mg-Cu alloys have received most attention and a yield stress up to 1 GPa has been reported by Liddicoat et al. [17].

There are three possible strategies to combine an UFG structure with nanoscaled precipitates using SPD techniques. Precipitates can be nucleated before, during or after the large straining that induces grain refinement. In aluminum alloys, this grain refinement results from dynamic recrystallization mechanisms [27,28] resulting from continuous generation and annihilation of dislocations leading to the formation of sub-grain boundaries and progressively to new grain boundaries with large misorientations [28–30]. In Al alloys, grain sizes in a range of 50 to 300 nm are typically achieved during room temperature SPD processing [3,12,19,20,23,25,31–33]. The final grain size depends on processing parameters (total strain, temperature, strain rate, etc.) but can also be influenced by metallurgical factors such as allowing elements [34], impurities or particles [13,35]. Thus, processing a heat treatable Al alloy in the solutionized state or precipitated state could give rise to different microstructures. It seems however that there is no systematic trend, since for example, Cepeda-Jiménez et al [9] have demonstrated that the grain size reached in an Al-7%Si alloy subjected to SPD is significantly smaller if the Si solute is in solid solution while Feng et al [18] have shown that stronger grain refinement was achieved in an Al-Cu-Mg alloy from a precipitated initial state. However, in the latter case, it has been shown that nanoscaled particles could be significantly damaged by large straining and partly dissolved even at room temperature [7,12,26,36,37]. Therefore, the most popular strategy to combine an UFG structure with nanoscaled precipitates is to process at first by SPD the solid solution treated alloy and then to apply a precipitation treatment. In few cases, some strain induced partial decomposition of solid solutions have been reported at room temperature, leading to GB segregations [17,36,38], GP-zones formation [15,19], clustering [37,39] or even the precipitation of stable phases [16,20,40]. At higher temperatures, dynamic precipitation processes are generalized and kinetics can be up to one or two orders of magnitude faster than during static annealing [5,8,11,15]. Such features are usually attributed to an enhanced atomic mobility related to deformation-induced vacancies and dislocations while GBs could act as preferential nucleation sites and fast diffusion paths [41]. For similar reasons, the precipitation of second phase particles in UFG structures during post-processing annealing treatments is usually much faster than in coarse grain materials [4,5,5,11,15,15,19,20,42–45], and some of the metastable phases of complex precipitation sequences do not appear anymore [10,46].

Beyond these differences in the precipitation mechanisms resulting from the specificity of UFG structures, the evolution of such unstable microstructures during annealing raises the more

general question of the competition between precipitation, grain growth and recrystallization. All these changes are driven by the minimization of the free energy of the system but connected to three different factors, the chemical driving force, the grain boundary energy and the dislocation density respectively. The atomic mobility and the mobility of defects drive the kinetics and will be dominant for these competing mechanisms. However, a specific complexity arises from heterogeneous precipitation that is very likely to occur along GBs or dislocations, as it should significantly affect the mobility of these defects. Initial GB segregations (if any), or solute drag at moving defects (GBs or dislocations) will promote these interactions, but in any case, they are probably positive since they should help stabilizing the UFG structure. Another important aspect of these complex microstructural evolutions is how to control and optimize the precipitate distribution in a situation where the proportion of GBs is enormous. It is well known in Al alloys that fast recovery of vacancies along GBs typically gives rise to precipitate free zones (PFZ). Besides, if mostly heterogeneous precipitation occurs, the question arises whether it remains possible to strengthen submicrometer grains by the classical precipitate hardening mechanism. More generally, open questions remain about the way to combine in an optimal way precipitate and GBs to hinder dislocation motion, about the contribution to strength of heterogeneously nucleated precipitates, and about the capability of such created UFG structures to provide enough strain hardening to give rise to sufficient uniform elongation under tension.

The aim of this work was to systematically investigate the influence of a high density of defects on the precipitation behavior in an Al-Zn-Mg-Cu alloy, with a special emphasis on the role of GBs. A UFG structure was obtained by high pressure torsion (HPT) at room temperature from the solutionized state, and post-processing ageing heat treatments were carried out to investigate the precipitation kinetics using complementary global and local characterization techniques such as : i) in-situ small-angle X-ray scattering (SAXS) which allows to follow the size and the fraction of precipitates in a large volume during heating; ii) differential scanning calorimetry (DSC) which provides a global view of the microstructure evolution during heating ; iii) transmission electron microscopy (TEM) for the observation of the precipitates location, size, fraction and the evolution of the grain size before and after annealing ; iv) atom probe tomography (APT) allowing to measure locally the solute content. Beyond the detailed understanding of precipitation mechanisms and the competition with recrystallization and recovery processes, the systematic relationship between microstructural features and the mechanical behavior was studied.

2. Material and Experimental methods

The Al-Zn-Mg-Cu alloy used in this study contains the major alloying elements 8.6% Zn, 2.5% Cu and 2.1% Mg with the other elements 0.4%Fe, 0.1% Zr and 0.04% Si (all in wt%). The alloy was received in the form of 5 cm diameter and 10 cm height cylinder after homogenization from Constellium C-TEC. To allow a post-deformation precipitation, the alloy was solution treated for 1h at 474°C. Following the solution treatment, the sample was directly brought to an ice-box to prevent natural ageing before deformation. The deformed samples were then kept as much as possible in a freezer; however, they were exposed to room temperature during traveling between the laboratories and during sample preparation, and this led to natural ageing between one and two weeks in total for all samples, un-deformed and deformed. The post-deformation natural ageing has a significant effect on the material's hardness (and therefore on its microstructure) (Supplementary material S1). SPD was carried out using HPT under a pressure of 6GPa up to 10

revolutions at room temperature with a rotation speed of 1rpm. Deformed samples were discs of 10mm diameter and 1mm thickness.

If we consider that the dimensions of the sample remain constant, and that the compression strain can be neglected, then the shear strain during HPT is given by [47]:

$$\gamma = \frac{2\pi N r}{h} \quad (1)$$

where N is the number of revolutions, r is the distance from the disc center and h is the thickness of the disc.

Shear deformation is therefore not homogeneous, it is maximum at the edge and theoretically zero in the disc center. This inhomogeneity of the deformation is typical of the HPT process [48–50]. This inhomogeneity is visible in the microhardness radial profiles (Supplementary material S1). In order to always characterize material subjected to the same level of deformation, all samples were taken at a distance of 2.5mm from the center of the HPT disc, where the shear deformation is $\gamma \approx 200$.

Mechanical properties were evaluated using tensile tests. Dogbone-shaped specimens were cut from the HPT discs using an electrical spark discharge machine (EDM). Miniature tensile specimens had gauge dimensions of 1.5 mm length, 0.7 mm width and between 0.5 to 0.7 mm thickness, and this gauge area corresponds to the position 2.5 mm away from the center of the HPT disc. Each tensile specimen was mounted horizontally on grips and pulled to failure with an initial strain rate of 3.10^{-3} s^{-1} using a testing machine operating at a constant rate of cross-head displacement.

TEM samples were prepared from 3mm diameter discs and thinned by electro-polishing (Struers TenuPol-5) with a mixture of 30% HNO_3 + 70%CH_3OH at a temperature of 243 K. Scanning TEM (STEM) was performed using a JEOL ARM-200F instrument operated at 200 kV. Dark Field (DF - collection angles 20–80 mrad) and high-angle annular dark field (HAADF – collection angles 80–180 mrad) images were recorded with a probe size of 0.2 nm and a convergence angle of 34 mrad. Additional analytical data were recorded by energy dispersive spectroscopy (EDS) with an Oxford Instruments X-max detector, which has a solid angle of 0.7 sr. Additional data were obtained with a JEOL 2100F microscope equipped with ASTAR automated crystal orientation mapping using scanning precession electron diffraction (SPED) (angle of 1.2°) [49–51]. Thanks to the SPED, orientation maps and the kernel average misorientation (KAM) maps were obtained. KAM parameter was used to study the distribution of local disorientations inside grains or sub-grains (here below a disorientation angle of 10°) and to calculate the dislocation density [52]. The geometrically necessary dislocation density ρ_{GND} was estimated from the mean degree of disorientation θ obtained in KAM [52,53]:

$$\rho_{GND} = \frac{\alpha\,\theta}{b\,d} \quad (2)$$

with α a constant between 2 and 4 depending on the dislocation type (an average of 3 is often chosen [53–55]), b=0.286 nm the Burgers vector and d the acquisition step of the map. In this study, we used α = 3.

Until now, measuring dislocations density by KAM has often been reported for EBSD studies [53–55]. In the present work, we extended this approach to TEM mapping which is needed in the case of very small grains structure.

APT analyzes were carried out using a CAMECA LEAP-4000HR instrument. APT tips were prepared using electro-polishing (electrolyte: 98% $C_8H_{16}O_3$ + 2% $HClO_4$). Samples were field evaporated at 40K in ultra-high vacuum (10^{-11} mbar) with electric pulses (pulse fraction of 20%, repetition rate 200kHz) at a detection rate of 0.2%. Data processing was performed with Gpm3dSoft software.

DSC measurements were carried out with a Mettler Toledo DSC 3+ instrument at a heating rate of 20 °C/min up to 500 °C. Samples were placed in pure Al crucibles with a capacity of 40 µl able to receive samples with an average size of 3*3*1 mm (cut out at 2.5mm from the HPT disc center) and a weight between 30 and 50 mg.

Small angle X-ray scattering (SAXS) measurements were performed on a custom-built laboratory setup with a rotating anode source at the K_α energy of Cu (wavelength of 0.154 nm) and a Pilatus 2D detector. SAXS patterns were background corrected, normalized to incident photon flux and sample transmission and thickness, and finally normalized to absolute units using a glassy carbon standard. *In situ* experiments were carried out using a dedicated furnace in which the samples, thinned to 70–100 µm, were placed. The diameter of the X-ray beam was 1 mm, and the signal was recorded from a location placed at the mid-distance between the center and the edge of the HPT-processed disc in order to probe a reproducible microstructure and to be able to correlate this data with STEM observations.

A usual strategy for SAXS data interpretation in precipitation system where objects cannot be considered as mono-disperse is to assume a parametric shape for the size distribution which can then be fitted to the experimental pattern. Since in our alloys we are expecting a rather wide size distribution and different populations of nanometric precipitates (intra-granular and inter-granular) we chose an assumption-free method to recover the actual size distribution.

For this we used a custom-implemented version of the McSAS software [56,57] which uses a Monte-Carlo algorithm to recover the size distribution. A detailed description of this software can be found in the references above, but we shall briefly recall the main features of the algorithm.

In order to recover the size distribution, the shape of the precipitates must be known. In our case, we will assume spherical precipitates, keeping in mind that small deviations on sphericity will be compensated in a way by a widening of the size distribution.

The principle of the algorithm is fairly simple. It consists in considering an assembly of N precipitates and to compute their resulting calculated SAXS signal which is then linearly scaled to the experimental data. The agreement with the experimental data is computed through the value of χ^2. The algorithm then picks a precipitate and changes its size. The resulting signal is re-calculated. If the agreement with the experimental data is better, then the change is accepted. This is repeated until the calculated signal matches the experimental signal within experimental uncertainties. A size distribution histogram is then computed with the final sizes of the N precipitates.

For a better representativity of the size distribution, we will display it as a volume weighted size distribution, which should be understood as a contribution of each size bin to the total integrated

intensity. To convert this to an actual volume fraction, we need to define the electronic contrast $\Delta\rho$ of the precipitates which can be expressed:

$$\Delta\rho = \frac{1}{\Omega} \sum_{i}^{\text{solutes}} (f_i - f_{Al})(C_i^p - C_i^m) \quad (3)$$

f_i and f_{Al} the scattering factors (which are equal to the atomic numbers in this case), Ω the atomic volume (16.5 Å^3) and C_i^p and C_i^m are the compositions of element i in the precipitates and in the matrix respectively. In this case, the compositions were given by APT as discussed in the next section.

Because the electronic contrast is different for the different phases (GP-zones and η'/η precipitates), we chose to represent the size distributions as a relative contribution to the integrated intensity. When volume fractions need to be extracted, a size threshold of 2 nm is used and the contribution of the objects below the threshold will be considered for calculating the volume fraction of GP-zones, and the contribution of objects above the threshold will be considered for calculating the volume fraction of η'/η precipitates.

3. Results

3.1. Ultrafine grain structure after severe plastic deformation

ASTAR automated crystal orientation mapping on the as-deformed alloy (Figure 1(a)) shows that an ultrafine grain structure with a grain size of less than 500 nm was obtained under a shear strain of $\gamma \approx 200$. The measured average grain size is 210 ± 50 nm, this is consistent with data reported for 7xxx series Al alloys deformed by SPD, as described in the introduction. It should be noted however that the measured grain size distribution (Figure 1(b)) exhibits a very wide distribution, from 20 to 250 nm. Besides, in the orientation map (Figure 1 (a)) misorientations are also present within the grains. This is confirmed by KAM map (Figure 1(c)) which highlights intra-granular disorientations (angle < 10°), and by the misorientation angle distribution (Figure 1 (d)). This distribution shows also a large fraction of high angle grain boundaries, as expected after severe plastic deformation [30,35].

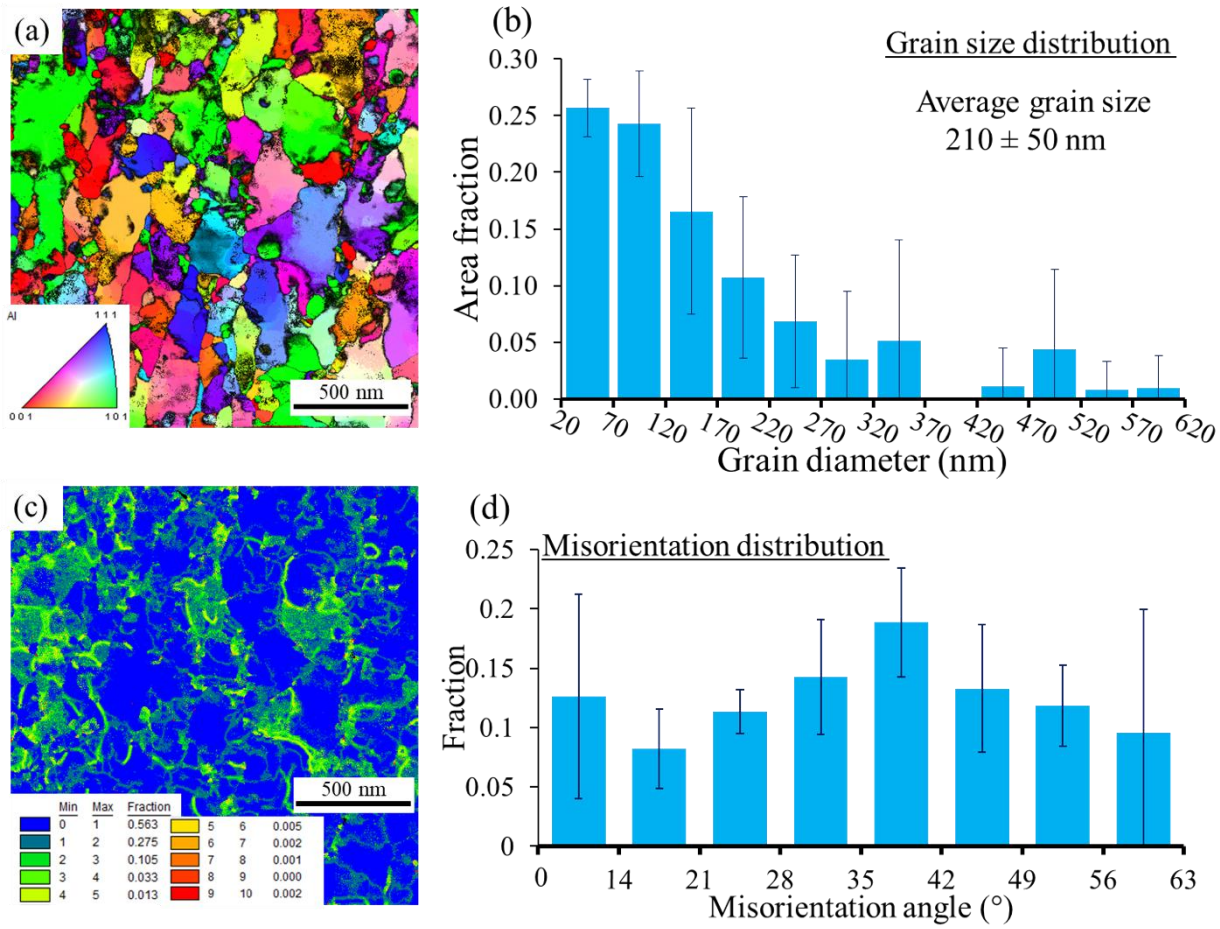

Figure 1: Orientation map (a), Kernel Average Misorientation (KAM) map (c), grain size (b) and misorientation angle (d) distributions of the as-deformed material.

Before deformation, the material was in the solid solution state, however, as shown on the STEM-HAADF images with a typical Z contrast (Figure 2(a)), some chemical heterogeneities are exhibited in the as-deformed state. There are some segregations along boundaries (arrowed on Figure 2(a)) and few nanoscaled precipitates (circled in Figure 2(a)) that contain a significant amount of solute (Zn, Cu or Zr which have a higher atomic number than Al). To quantify these segregations, EDS measurements were carried out (Figure 2(b)). The line profile shows that segregated solutes are mainly Zn together with a small fraction of Mg. More precise quantification was also performed thanks to APT analyses with a higher sensitivity. A boundary was intercepted in the volume displayed on Figure 2(c) and the profile computed across confirmed the segregation of Zn, Mg but indicates a small Cu enrichment also (Figure 2(d)).

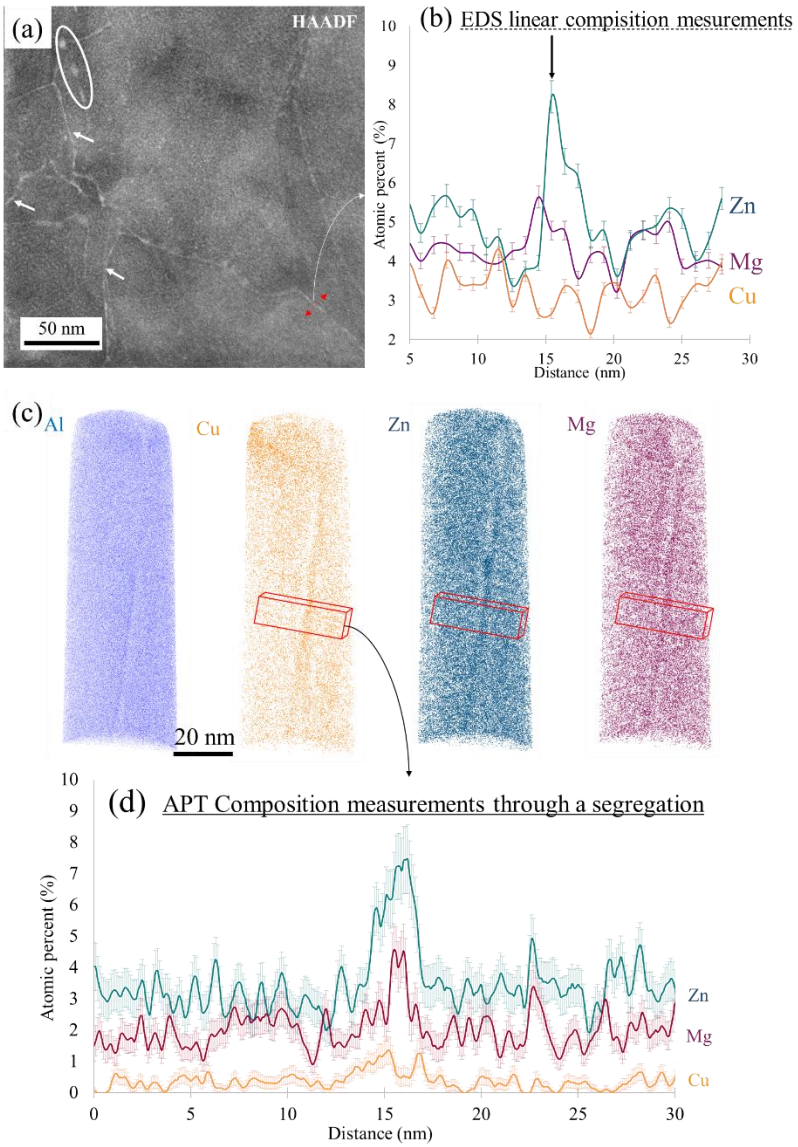

*Figure 2: As-deformed material STEM-HAADF(a) image and EDS linear composition scan through a segregation (b). 3D reconstruction of volumes analyzed by APT (c) and APT 3D composition measurements through a segregation (d) using boxe of 10*5*30nm.*

Al-Zn-Cu-Mg alloys typically exhibit GP-zones in naturally aged samples and such features were also detected in APT data set collected in the un-deformed alloy (Figure 3 (a)). Their size, composition and volume fraction was estimated using the Isoposition method (IPM) [58]. In the deformed state (Figure 3(b)), GP zones also appear but the quantification using the Iso-position method was carefully calibrated to discriminate solute segregations from precipitates. To do so, the level of several boundary segregations was measured, and a composition threshold was set just above the measured composition (Zn 10 at% and Mg 5 at%) to extract GP zones. Additionally, only particles containing more than 50 atoms were considered. Then, erosion profiles were computed and as shown on Figure 3(c), precipitates do not exhibit any composition plateau in the core. Thus, to estimate their size and composition, interfaces with the matrix were considered at a location where the solute concentration reaches 50% of the maximum. The obtained quantitative results are listed in Table. 1. These data, including erosion profiles and 3D

reconstruction (Figure 3) highlight two populations of precipitates: one with a mean radius < 2 nm, which can be identified as GP-zones [59,60], and a second with a diameter of about 10nm and a higher solute concentration which can be identified as η' or η precipitates [60]. The first population appears to be distributed homogeneously and is similar to that of the un-deformed alloy while larger precipitates were only detected in the deformed alloy. They are located along grain or sub-grain boundaries covered by solute segregations. These zones and precipitates may have formed both during the deformation process and during the subsequent natural ageing.

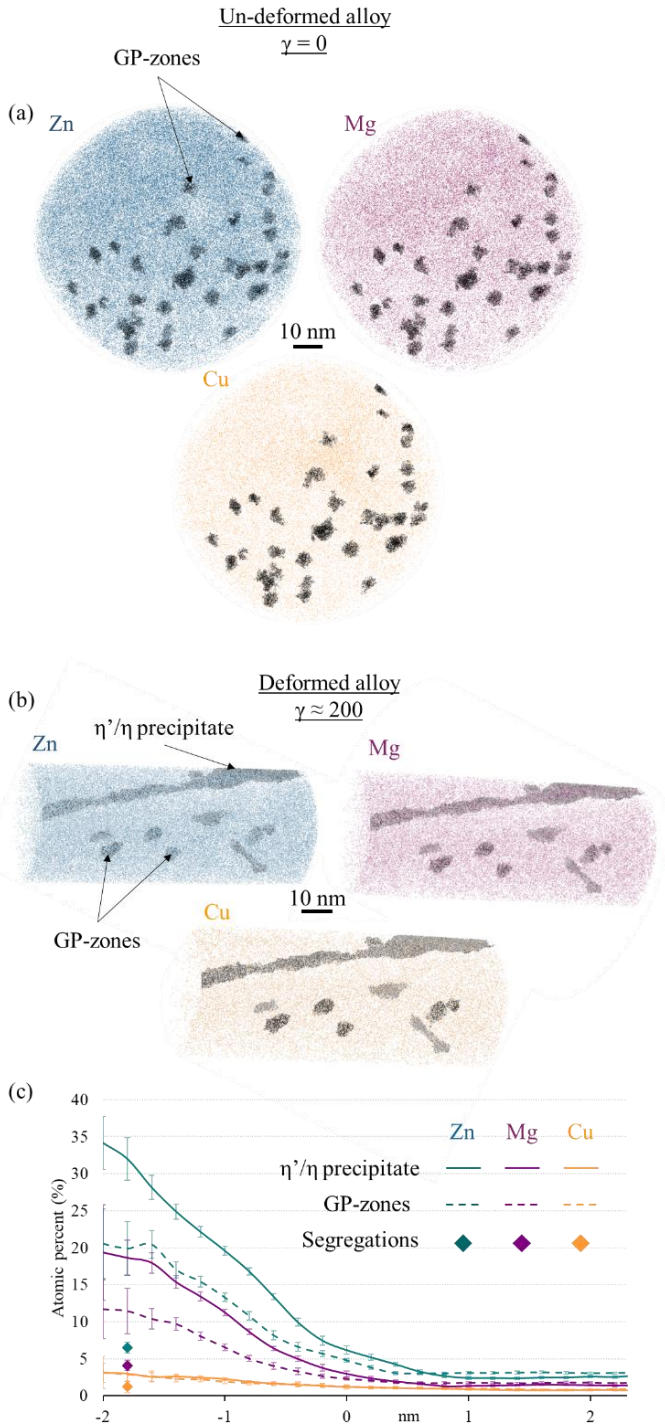

Figure 3 : 3D reconstruction of volumes analyzed by APT in the un-deformed (a) and HPT deformed (b) materials. Graphic presenting the erosion profile of precipitate identify as GP-zones (dashed lines) and η'/η (solid line) to characterize precipitates composition and the composition of a segregation (diamond-shaped markers) (c).

The matrix composition was measured from APT data by removing precipitates (including matrix/precipitates interfacial zones) and segregations. These measurements show that, 3.06 %; 1.83 % and 0.83 % of atomic Zn, Mg and Cu respectively are still in solid solution after deformation. These values are not so different from the un-deformed alloy (Table. 1).

	Zn at.%	Mg at.%	Cu at.%
Matrix γ = 0	**3.45 ± 0.02**	**1.79 ± 0.02**	**0.88 ± 0.01**
Matrix γ ≈ 200	3.06 ± 0.02	1.83 ± 0.01	0.83 ± 0.01
GP-zones γ = 0	**13.49 ± 1.20**	**5.11 ± 1.25**	**1.17 ± 0.61**
GP-zones γ ≈ 200	17.59 ± 8.92	7.31 ± 4.31	2.56 ± 1.64
η'/η precipitates γ ≈ 200	24.34 ± 1.02	15.08 ± 0.85	2.59 ± 0.38

Table. 1: APT measured in Zn, Mg and Cu of matrix and of the different populations of precipitates for un-deformed and deformed Al-Zn-Mg-Cu alloy.

To confirm APT analyses, SAXS measurements were carried out to quantify the precipitate size distribution and volume fraction. Data collected at room temperature (Figure 4(a, b)) show the size distribution of precipitates in the un-deformed and deformed (after 10 turns of HPT) alloys. The un-deformed alloy (dashed line) shows two populations of precipitates after solution treatment. The first population shows radiuses between 0.4 and 1 nm (GP-zones) and the second between 7 and 14 nm but with a much lower volume fraction. The curve from the deformed alloy (solid line), shows the same two populations of precipitates with a lower volume fraction, as well as a third population with radiuses between 1.5 and 4 nm. Other precipitates of even larger size may be overlooked by this SAXS characterization, since the set-up used in this study does not allow to detect precipitates larger than 15nm.

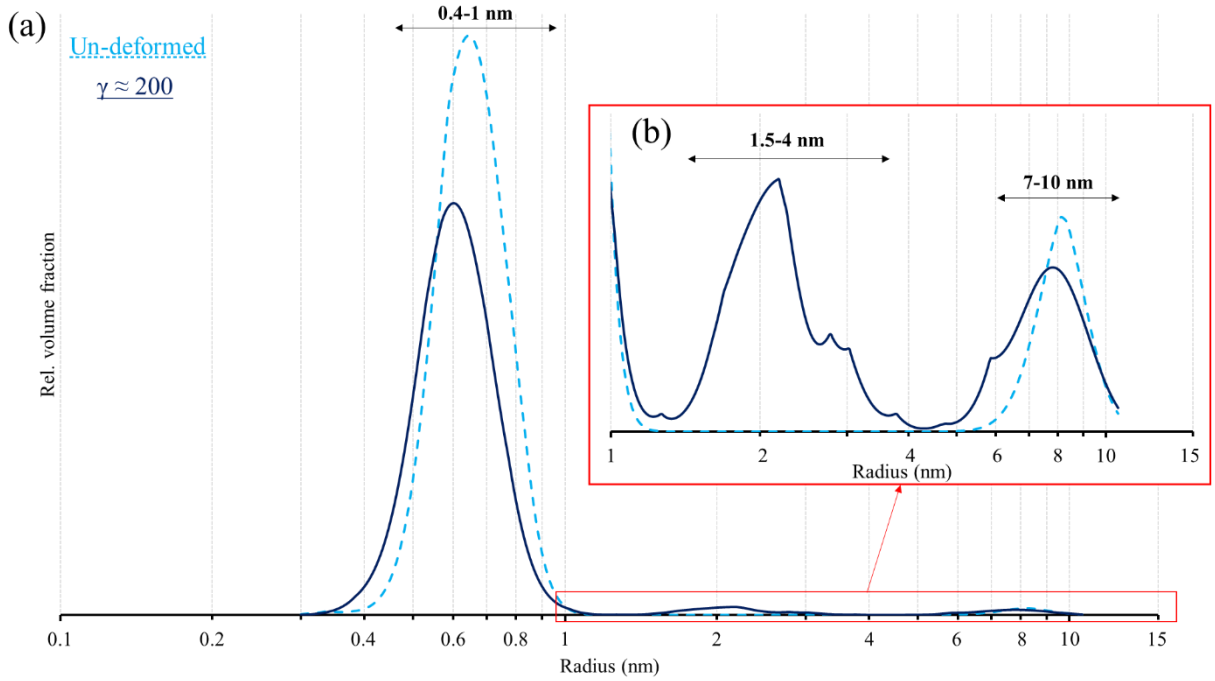

Figure 4: (a)Precipitate size distribution calculated from SAXS data fitting for the un-deformed (dashed line) and deformed (solid line) materials at 25°C. (b)enlargement of identified area.

The GP-zones and the η'/η precipitates highlighted by the APT and STEM observations are in agreement with the precipitate size distribution determined by SAXS. In addition, APT and

STEM demonstrate that the η'/η precipitates results from strain induced heterogeneous precipitation at grain and sub-grain boundaries.

3.2. Microstructure evolution during ageing

Materials deformed by SPD are very sensitive to heat treatment in terms of grain growth and precipitation. Thus, to observe the progressive microstructure evolution including the first stage of precipitation in the deformed material an optimal ageing temperature should be selected. Therefore, a preliminary study applying a temperature ramp was carried out using DSC and SAXS analyses, aiming at defining the temperatures for further isothermal annealing.

The monitoring of precipitation kinetics during annealing of the un-deformed and the deformed alloys was first carried out by DSC in order to obtain a global view of the microstructure evolution kinetics (Figure 5). The comparison between as-deformed and un-deformed materials, shows that the first endothermic peak, which corresponds to the dissolution of GP-zones, has a much lower intensity in the deformed material and is shifted to a lower temperature (from 120°C down to 90°C). According to previous work [61], the diminution of the area under this peak could correspond to the presence of lower volume fraction of GP-zones before annealing. Another possibility would be an overlap between GP-zones dissolution and crystalline defect recovery or precipitation of subsequent phases.

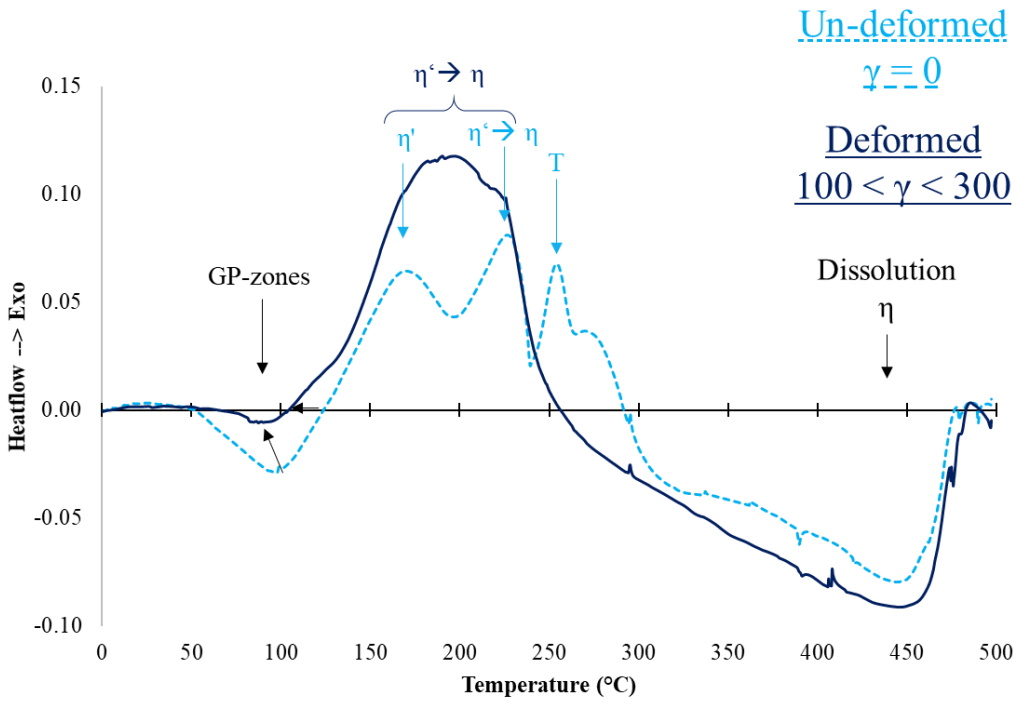

Figure 5 : DSC thermograms of the un-deformed (dashed line) and deformed (solid line) materials subjected to a heating ramp of 20°C/min.

The next exothermic peaks of the un-deformed alloy correspond, first at 170°C, to the formation of the metastable η', followed by other peaks at 220°C and 250°C, related to the complex transformations from η' to the stable phase η [15,42], and probably to the nucleation and growth of T($Al_2Mg_3Zn_3$)phase [42]. A detailed study of the reactions taking place above 200°C was

beyond the scope of this work (i.e., outside of the temperature ranges of interest) and was not investigated. In the deformed material, all this complex precipitation sequence merges in one broad exother1mic peak, shifted to lower temperature (onset shifted from 150°C down to 100°C). These data strongly suggest that the transition from GP-zones to equilibrium phases is promoted in the deformed material and happens at lower temperature.

This influence of the deformation on the precipitate evolution has been quantified by *in-situ* SAXS, using a lower heating rate (0.5 °C/min) to guarantee a sufficient acquisition time. Precipitate size distributions (PSD in radius) were calculated from the SAXS data collected during the heating ramp. They are presented as a function of temperature as contour plots in Figure 6(a) and (b) for the un-deformed and deformed materials respectively. In the un-deformed material, a decrease of the intensity of the PSD is observed in a first stage with no significant change of the precipitate radius (up to about 100°C). This stage corresponds to the dissolution of GP-zones revealed by DSC. Then, a continuous evolution towards larger precipitates is exhibited, between 120 and 200°C. It corresponds to the exothermic precipitation stage of η' also pointed out by DSC. In the deformed alloy, the evolution of GP-zones is qualitatively comparable. However, the transition towards larger precipitates is much more disruptive. It happens at lower temperature (below 100°C), and is finished within the size range measurable by SAXS at about 150°C. A more precise view can be obtained by plotting PSD and the fraction evolution considering two populations of precipitates (Figure 6(c- f)).

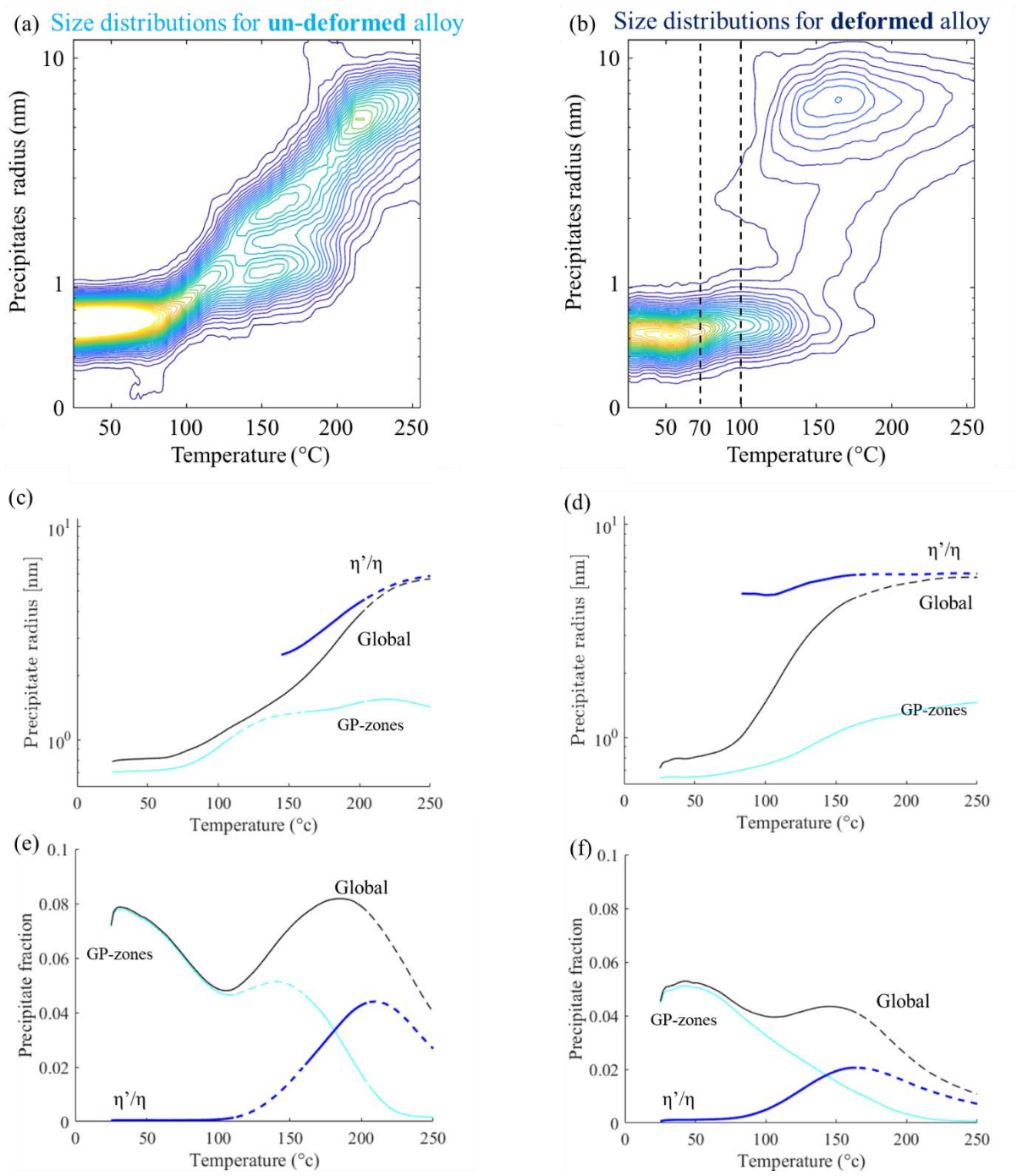

Figure 6: Precipitates radius distribution estimated from SAXS data fitting during an in-situ heating at 5°C/min from 20 to 250°C on un-deformed (a) and deformed (b) alloy. Precipitates average radius evolution (c, d), and precipitates fraction evolution (integrate intensity of SAXS data) (e, f) in function of temperature for un-deformed (c, e) and deformed alloys (d, f). In (c-f) graphics, the precipitates are separated in two populations considered as GP-zones (>2nm) and η'/η (>2nm). Dashed line correspond to low data confidence regions that come from detection limit (10nm precipitates radius).

At 120°C (Figure 6(c-f)), where the DSC curves show a dissolution of the GP-zones, the magnitude of the PSD obtained from SAXS is halved for both the un-deformed and deformed materials. However, there is a different evolution of the size of these GP-zones between the un-deformed and the deformed alloy. The average size of the GP-zones increases from 0.6 nm to 1.2

nm for the un-deformed sample but evolves more slowly for the deformed alloy. However, the most significant difference between the initial states lies in the larger precipitates. For the deformed alloy, the size of η'/η precipitates is stable with a wide distribution ranging from 1.7 to 14 nm (average near 6nm) and their fraction increases early (from 70°C). This population does not exist at this stage in the un-deformed sample.

At 150°C, the DSC curves (Figure 5) of un-deformed alloy showed the beginning of η' phase precipitation. On the PSD obtained from SAXS (Figure 6(c, e)), the GP-zones dissolution continues after a slight increase in the fraction and a second population slightly above 2 nm appears, which can therefore be identified as the nucleation size of η'. The increase of GP-zones fraction between 110°C and 150°C is probably due to fine η' precipitates accidently included with the GP-zone (dashed line in Figure 6(c, e)). For the deformed alloy (Figure 6(d, f)), a similar coexistence between GP-zones (without the slight increase in fraction) and new η' is found however with much lower volume fraction.

At 200°C (Figure 6(c, e)), for the un-deformed alloy, the dissolution of GP-zones is almost finished. In parallel, the size of the precipitates has grown up to about 5 nm. In the deformed alloy (Figure 6(d, f)), the distribution of large precipitates seems to be relatively stable as compared to 150°C, however the decreasing volume fraction suggests the presence of larger precipitates whose mean size is above the observation range of SAXS. At 220°C, a single precipitate population, with an average radius of about 6 nm, is measured for both alloys. Again, the volume fraction is much larger for the un-deformed alloy, suggesting the presence of undetectable larger particles in the deformed alloy (represented by dashed line on Figure 6(c- f)).

In summary, SAXS results show that precipitates in the deformed alloy grow more rapidly than in the un-deformed alloy when the temperature increases. There are several populations with different sizes with volume fractions varying with the temperature.

This first approach shows that the nucleation of a high density of nanoscaled precipitates in the deformed material requires a significant decrease of the temperature as compared to the classical T6 thermal treatment (120°C-160°C). This is of particular importance to consider the fastest precipitation kinetic and to avoid a fast transformation of the deformed microstructure, which would also in turn reduce yield strength contributions. In the following, we have selected two temperatures for isothermal treatments, as indicated on Figure 6(b): 70°C, which is the temperature just before the formation of the large size precipitates, and 100°C, which is the temperature for which these large precipitates start to grow.

3.3. Microstructure evolution during isothermal ageing

Figure 7 shows the orientation maps, KAM maps and grain size distributions of the deformed material after thermal ageing at 70 and 100°C. The orientation map of the deformed alloy after 70h at 70°C (Figure 7(a)) shows that the grain size seems to decrease or at least remains stable as compared to the as-deformed state. KAM maps (Figure 7(b)) show a decrease of the small disorientations. Using eq. (2), this is consistent with a diminution trend of the dislocations density: from $4.2 \times 10^{15} \pm 2.1 \times 10^{15}$ m^{-2} to $2.8 \times 10^{15} \pm 1.3 \times 10^{15}$ m^{-2}.

Even after 48 h at 100°C, the orientation map of the deformed alloy (Figure 7(c)) shows that a grain size smaller than 500 nm is retained. KAM map (Figure 7(d)) also shows a decrease in

intra-granular disorientation with annealing, relatively similar to that observed after annealing at 70°C. The estimated dislocation density (from eq.(2)) is $2.8x10^{15}\pm0.7x10^{15}$ m^{-2}.

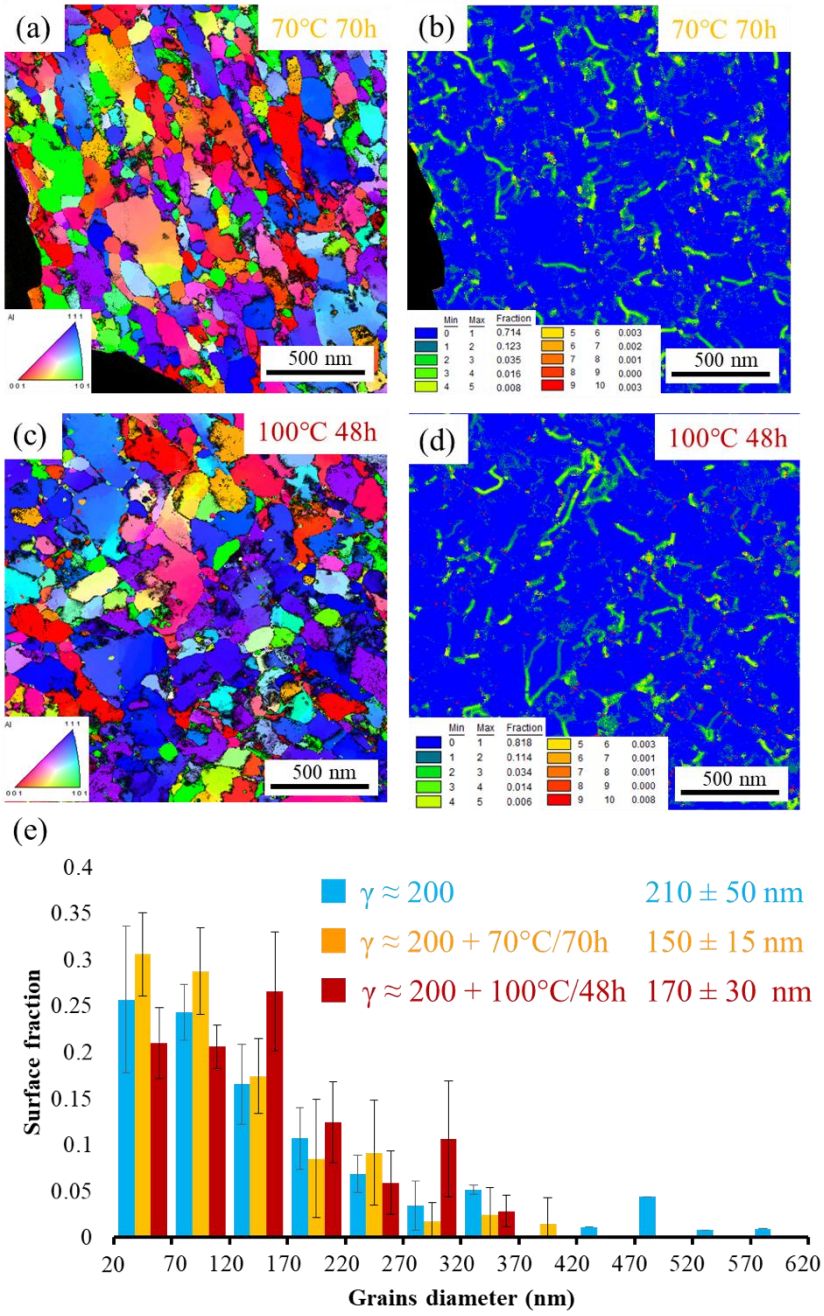

Figure 7 : TEM orientation maps (a, c) and KAM maps (b, d) of the deformed material after thermal treatments at 70°C/70h (a, b) and 100°C/48h (c, d). And (c) surface grain size distributions for the deformed material before and after thermal treatment at 70°C/70h and at 100°C/48h.

Grain size distributions (in surface fractions) were extracted from these orientation maps and are plotted in Figure 7(e) as. Number density distributions, as well as misorientation distributions, are provided as supplementary material (S2). These results show that the grain size distribution is shifted towards significantly smaller values (mean size from 210 ± 50 down to 150 ± 15 nm) and narrower after annealing at 70°C/70h. This seems to indicate that recovery or at least partial

recrystallization probably occurred. After annealing at 100°C, the mean grain size is 170 ± 30 nm, still smaller than that of the as-deformed material. The disorientation angle distributions (supplementary material S2) shows high density of high angle grain boundaries for deformed and annealed alloys. The only difference between the three states is the significantly higher fraction of disorientation < 15° for the alloy annealed at 70°C. This could be explained by a re-organization of dislocations in a dislocation wall meaning a partial recrystallization. However, the important point is that annealing (up to 100°C) does not lead to rapid grain growth.

In order to follow the evolution of the precipitates during isothermal heat treatments at 70°C and 100°C, the PSDs and the precipitates fraction evolution extracted from the SAXS data were plotted (Figure 8 and Figure 9).

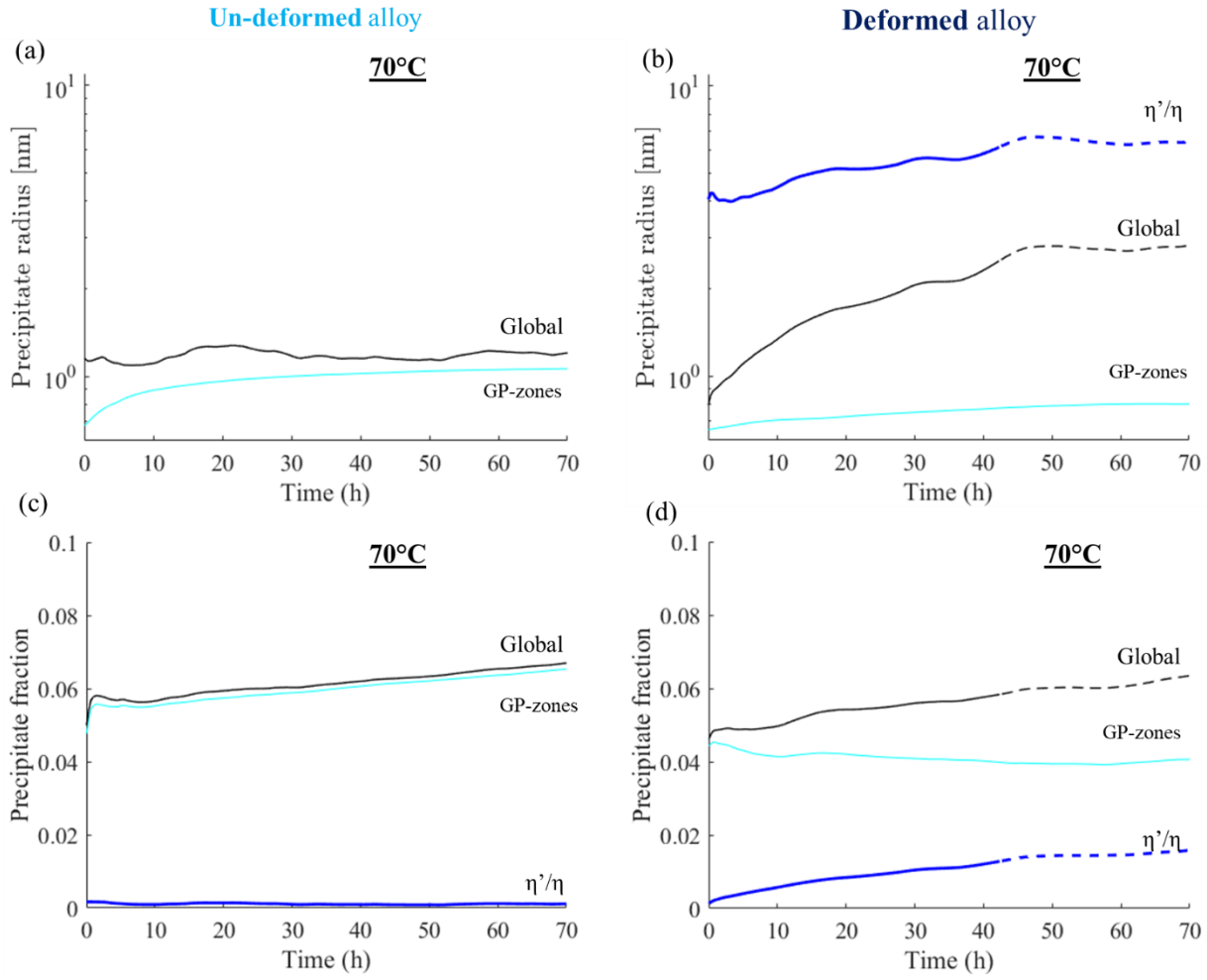

Figure 8 : Precipitates size distribution (a, b) and fraction evolution (c, d) estimated from SAXS data fitting during in-situ heating at 70°C on un-deformed (a, c) and deformed (b, d) alloys. Dashed lines correspond to evolution of global size and fraction of precipitates and solid lines to evolution of fraction and size of precipitates separates in two populations: GP-zones and η'/η.

At 70°C, the evolution of the GP-zones is similar in the two materials, with a very slow evolution of the radius up to about 1 nm. The volume fraction of GP zones is relatively constant in the un-deformed material, while it slightly decreases with time in the deformed material. This

diminution is related to the growth of larger precipitates, as observed at 120°C during ramp heating. However, at this low ageing temperature (70°C), the volume fraction of such large precipitates remains very low. As the current SAXS configuration allows only to observe precipitates whose radius is below 10nm, it is possible that the stabilization of fraction and size evolution of η'/η precipitates was underestimated (dashed line in Figure 8(b, d)).

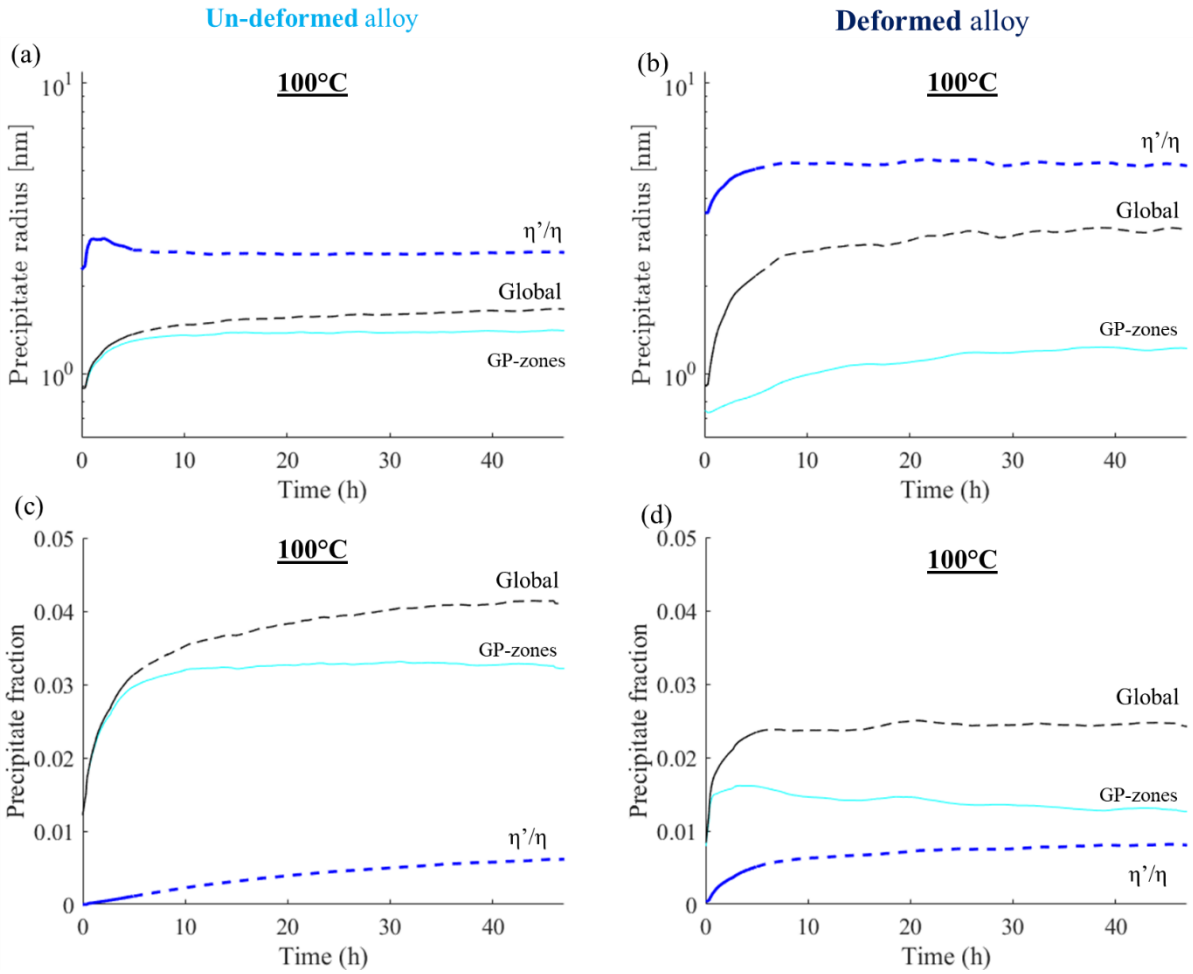

Figure 9 : Precipitates size distribution (a, b) and fraction evolution (c, d) estimated from SAXS data fitting during in-situ heating at 100°C on un-deformed (a, c) and deformed (b, d) alloys. Dashed lines correspond to evolution of global size and fraction of precipitates and solid lines to evolution of fraction and size of precipitates separates in two populations: GP-zones and η'/η. -

At 100°C, the behavior is qualitatively similar. In both materials a population of nanoscaled precipitates with a radius of about 2 nm (presumably η') is detected along with the growth of the pre-existing GP-zones. However, in the deformed material, the fraction of remaining GP zones is lower, and the population of large precipitates is both larger (average size: 4nm), and of larger fraction than during the treatment at 70°C. The evolution of size and fraction of η'/η precipitates can still be under-estimated during this ageing (dashed line in Figure 9 (a- d)).

A strange point, is that, at the beginning of the 100°C treatment (25°C), the fraction of GP-zones is 3 times higher than at the beginning of the 70°C treatment (25°C) (Figure 8 and Figure 9 (a,b)). This could be due to an effect of additional natural ageing or an overshoot of temperature

during the ramp heating to reach 70°C. The increase in GP-zones fraction is the same for the deformed and the un-deformed sample, suggesting that they have been subjected to the same thermal conditions. This point will be discussed in the following parts of this study.

Thus, in-situ SAXS measurements during isothermal heat treatment demonstrate the coexistence, in the deformed material, of small precipitates (GP-zones) behaving similarly to those of the un-deformed material, and of larger particles whose fraction increases with ageing time and with ageing temperature.

To confirm this analysis with direct observations, STEM-HAADF imaging has been performed after 70 h at 70°C in the deformed material (Figure 10(a)), after 48 h at 100°C in the deformed material (Figure 10(b)) and in the un-deformed material (Figure 10(c)). Additional STEM images are presented in supplementary material (S3).

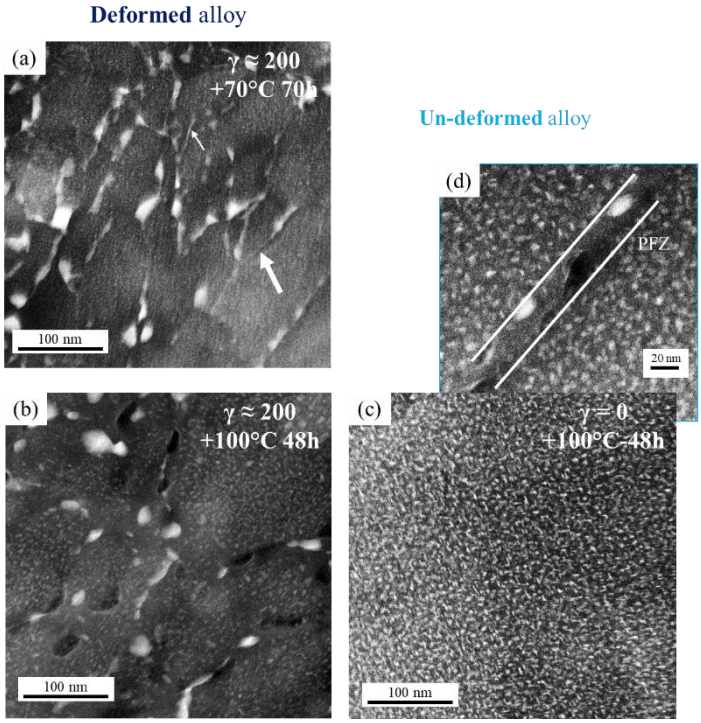

Figure 10 : STEM-HAADF images of deformed (a, b) and un-deformed (c,d) materials annealed 70h at 70°C (a) and 48h at 100°C (b, c, d).

The micrograph of the deformed alloy after 70°C/70h (Figure 10(a)) confirms that even at this relatively low temperature, a high density of precipitates nucleates and grows. In agreement with the SAXS data, two distinct precipitate populations are observed. The first appears on defects, mainly along boundaries, and it exhibits a wide radius distribution (2.5nm to 15nm, mean value 7nm). The second is intra-granular, with a typical size of the order of 1nm. Thus, these observations are in good agreement with the SAXS results. On STEM HAADF images, some bright lines clearly appear (arrows on Figure 10(a)). They could be the result of heterogeneous precipitation along boundaries or solute segregations such as before aging (Figure 3). Unfortunately, these samples turned out to be extremely sensitive and systematically gave rise to early specimen failure during APT analyses. Thus, no quantitative data could be collected by this technique to clarify these features.

The micrograph of the deformed alloy after 100°C/48h (Figure 10(b)) reveals numerous inter-granular precipitates with radius between 5 and 20 nm, thus slightly larger than after 70°C/70 h, as well as intra-granular precipitates (of radius: 1-1.5 nm). PFZ where intra-granular precipitates are absent clearly appear around the large precipitates. The largest precipitates observed in the micrograph are in principle not detected by the SAXS measurement, since their size is above the measured range. This intrinsic size limitation of SAXS accounts for the difference in size distribution as compared to TEM data.

For both heat treatments on the deformed alloy (70 and 100°C), inter and intra-granular precipitation occurred. Inter-granular precipitation was observed along every kind of boundary, with low or high angle misorientation. Consistently with the SAXS results, the 70°C heat treatment is more dominated by intra-granular precipitation as compared to the 100°C heat treatment.

The micrograph of the un-deformed alloy annealed at 100°C during 48h (Figure 10 (c)), shows that intra-granular precipitation took place during annealing and that the precipitates have a radius between 1 and 2.5 nm in agreement with SAXS and the literature data [62]. Figure 10(d) shows a grain boundary on which precipitates with a radius between 10 and 20 nm have nucleated. It looks very similar to inter-granular precipitation in the deformed material and thus clearly demonstrates the critical role played by boundaries as nucleation sites.

APT analyses were performed on the deformed material annealed at 100°C/48 h (Figure 11) to study the composition of the precipitates (Table.2). This 3D reconstruction shows intra-granular Zn and Mg (sometimes Cu) rich precipitates (2.6±0.6nm radius) and also one inter-granular precipitate (7.6 ± 1.3 nm radius). A PFZ is also visible in the vicinity of a planar feature attributed to a grain boundary. The measured precipitate compositions (summarized in Table.2) show that intra-granular precipitates have a composition close to those found in the as-deformed state (according to the literature, similar to the composition of classical GP-zones [59,63–65]). In inter-granular precipitates, the concentration of Zn, Mg and Cu has increased during annealing as compared to the as-deformed state: Zn 24 to 48 %at., Mg 15 to 35 %at. and Cu 3 to 6 %at. Such a composition corresponds to η' or η precipitates [65]. Besides, as expected, during annealing, there is a significant decrease of solute content in the matrix: from 3.1 to 1.9 %at. for Zn and from 1.8 to 1.1 %at. for Mg, while the Cu composition seems to remain stable.

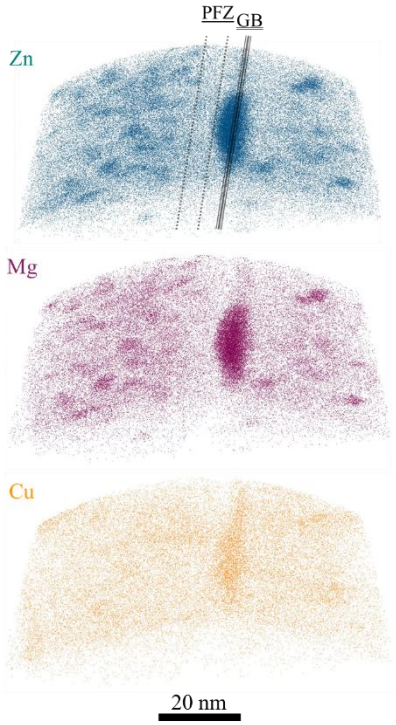

Figure 11 : 3D reconstruction of a volume analyzed by APT of the deformed material annealed at 100°C/48h.

This first part on precipitation behavior after deformation shows that, by adjusting the aging temperature, it is possible to achieve a fine distribution of nanoscaled precipitates with a tailored size, comparable to that of the un-deformed material in the T6 condition. However, the difference between un-deformed and deformed state is the presence of a second population of precipitate located at grain boundaries in the deformed state.

		Zn at.%	Mg at.%	Cu at.%
Matrix	**$\gamma = 0$**	**3.45 ± 0.02**	**1.79 ± 0.02**	**0.88 ± 0.01**
	$\gamma \approx 200$	3.06 ± 0.02	1.83 ± 0.01	0.83 ± 0.01
	$\gamma \approx 200$ +100°C/48h	1.88 ± 0.56	1.07 ± 0.15	1.07 ± 0.18
Intra-granular precipitates	**$\gamma = 0$**	**13.49 ± 1.20**	**5.11 ± 1.25**	**1.17 ± 0.61**
	$\gamma \approx 200$	17.59 ± 8.92	7.31 ± 4.31	2.56 ± 1.64
	$\gamma \approx 200$ +100°C/48h	14.29 ± 4.79	8.34 ± 5.02	1.94 ± 1.82
Inter-granular precipitates	$\gamma \approx 200$	24.34 ± 1.02	15.08 ± 0.85	2.59 ± 0.38
	$\gamma \approx 200$ +100°C/48h	47.67 ± 8.11	35.25 ± 1.39	5.48 ± 1.34

Table.2 : Composition in Zn, Mg and Cu of matrix and of the different populations of precipitates for un-deformed, deformed and annealed materials.

3.4. Mechanical properties

The mechanical properties of both un-deformed and deformed materials, before and after annealing at 70 and 100°C, have been measured by tensile tests (with samples of identical geometry for meaningful comparison). The tensile curves are presented in Figure 12. In micro-tensile tests, grain size can have an influence, if it is comparable to the dimension of section. That can give higher uncertainties compare to classical tensile tests. On large grain samples, the standard deviation of the stress measurement is max. ± 50 MPa and for small grain samples max. ± 40 MPa.

The tensile curve of the un-deformed alloy exhibits a yield stress (at 0.2%) of 240 MPa and a uniform elongation of 23.6±0.8 %. After deformation ($\gamma \approx 200$), as expected the yield stress is much higher, up to 770 MPa and the elongation to failure is reduced down to 9 ± 3 %.

Annealing at 70°C for 70h of the un-deformed alloy leads to a 90MPa shift of the yield stress as compared to the solutionized alloy (up to 330 MPa) and to a significant reduction of the elongation to failure (from 23.6 ± 0.8 down to 12 ± 0.5 %). For the alloy deformed before aging at 70°C during 70h, the yield stress increase is a bit less, about 70MPa (up to 850 MPa) but the elongation to failure remains relatively constant (6.7 ± 0.6 %).

After annealing at 100°C for 48h, the yield stress is up to 440MPa, significantly higher than after annealing at 70°C but the elongation to failure is down to only 5.4±0.5 %. This is in contrast with the behavior of the deformed alloy annealed in similar conditions, which exhibits a lower yield stress as compared to the 70°C treatment (800 vs. 850 MPa) and a larger elongation to failure (9.6 ± 1.4 % against 6.7 ± 0.6 %). All these experimental data are summarized in Table 3. It is important to note that the highest UTS which was achieved is extremely high for this type of alloy, it is indeed up to 960±20MPa obtained for the deformed sample after annealing at 70°C.

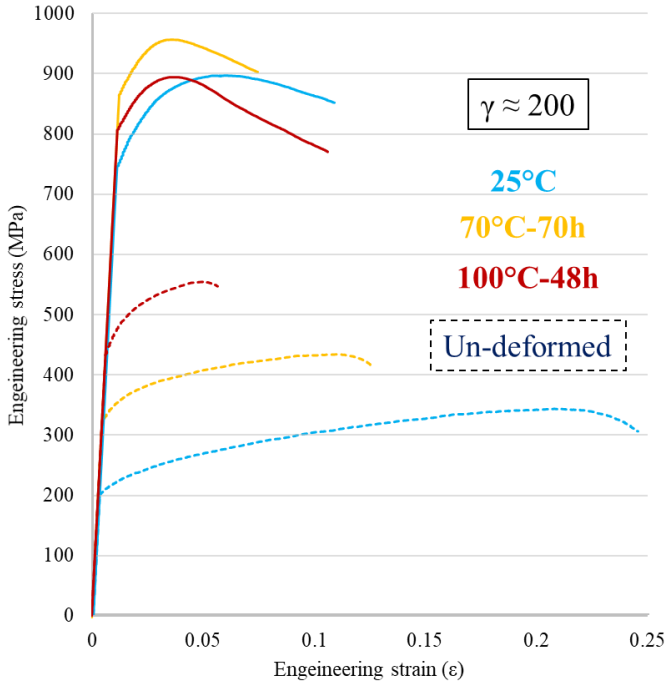

Figure 12: (a) Tensile curves of un-deformed (dashed line) and deformed (solid line) materials and after their annealing at 70°C/70h and after 100°C/48h.

	Yield stress			UTS			Elongation to failure		
	As SHT/deformed	70°C/70h	100°C/48h	As SHT/deformed	70°C/70h	100°C/48h	As SHT/deformed	70°C/70h	100°C/48h
Un-deformed	244 ± 52	334± 50	440± 50	354 ± 10	437 ± 10	510± 10	23.6 ± 0.8	12 ± 0.5	5.4 ± 0.5
γ ≈ 200	770 ± 23	850 ± 40	800 ± 22	882 ± 12	960 ± 20	902± 11	8.6 ± 3.0	6.7 ± 0.6	9.6 ± 1.4

Table. 3 : Yield strength, ultimate tensile strength and elongation to failure measurements for un-deformed and deformed materials and after their annealing at 70°C/70h and at 100°C/48h.

4. Discussion

4.1. Deformation induced microstructure

The deformation by HPT leads to a nano-structuration of the alloy, resulting in an important increase of the yield stress up to 770 MPa. A mean grain size of 210 ± 50 nm was achieved with high density of intra-granular defects resulting in local lattice distortions. Such a grain size is significantly larger than data usually reported in the literature for similar alloys deformed in equivalent conditions. For example, after 10 turns by HPT of an Al-Zn-Mg-Cu alloy, a grain size of 80 ± 20 nm was measured by TEM by Markushev and co-authors [25]. Using XRD, Islamgaliev et al. reported for a similar material a mean grain size below 100 nm [32]. This large difference probably results from the methodological approach. Indeed, from conventional TEM data or XRD, it is not possible to discriminate low angle GBs and high angle GBs (HAGB). In our experiments, using ASTAR automated crystal orientation mapping, the measured grain size really corresponds to HAGBs, such as for Transmission Kikuchi Diffraction [30].

In Al-Zn-Mg-Cu alloys, a high density of GP zones typically forms after the solution treatment during natural aging at room temperature. This phenomenon is promoted by the annihilation of excess vacancies that have a relatively high mobility at room temperature. In the deformed material, similar GP zones were detected by SAXS but with a smaller volume fraction as compared to the un-deformed state. This difference suggests that after plastic deformation, the overall atomic mobility driven by vacancy concentration and mobility is lower than after quenching. Since it has been proven that a high excess vacancy concentration exists during SPD [16,46,66], this indicates that these excess vacancies have quickly annihilated on the high density of crystalline defects (dislocations and grain boundaries) created during plastic straining.

Additionally, this high density of crystalline defects (dislocations and grain boundaries) created during plastic straining plays another important role on the solute distribution: they act as nucleation site (during deformation or natural aging) for η'or η particles and more generally they promote the local segregation of Zn, Mg and Cu. The formation of such segregations has been attributed to solute drag by moving defects: moving dislocations may drag solute atoms and transport them to grains boundaries [16]; grains boundaries motion may sweep solute atoms (snowplow effect [67]); vacancies may drag solutes with a positive binding energy toward GBs where they annihilate [37]. These mechanisms give rise to segregations but also lead to faster precipitation kinetics. Strain induced segregations have been reported for several systems and are usually more pronounced for higher strain level and higher temperatures [37,68,69].

4.2. Evolution of the nano-structure during ageing

DSC and SAXS analyses have shown that the severe deformation affects the precipitation sequence. On the DSC plot (Figure 5), the classical sequence GP-zones→η' and η'→η is merged in a single wide peak while SAXS data (Figure 6) demonstrated a much faster growth of precipitates. Besides, TEM and SAXS analyses indicate both that a bi-modal precipitate size distribution develops during low temperature annealing only in the deformed material. As discussed in the introduction, such a faster kinetics has already been reported for other severely deformed aluminum alloys and it has been attributed to: i)- strain induced excess vacancy concentration; -ii)- heterogeneous nucleation on structural defects; -iii)- accelerated diffusion along crystalline defects; iv)- solute drag by defect motion.

The STEM observations show that the bi-modal precipitate size distribution consists of a fine-scale population of intra-granular precipitates and larger precipitates located mainly on the grain and sub-grain boundaries. The population of small intra-granular precipitates is ideally characterized by SAXS data. The evolution of the precipitate radius distribution during ageing shows a progressive partial dissolution of the GP zones (radius ~ 1 nm), followed by the formation of slightly larger (radius ~ 2 nm) precipitates, which are presumably the η' phase. The kinetics of this process in terms of size evolution seems to be almost identical in the deformed and un-deformed materials, in agreement with an earlier study [19]. However, the volume fraction of these GP zones appears to be much smaller in the deformed material as compared to the un-deformed material, and it decreases with increasing temperature. This is supported by our TEM observations showing that regions with homogeneous intra-granular precipitation shrink between 70°C and 100°C ageing, with a precipitate-free zone (PFZ) developing around larger inter-granular precipitates. Then, since the population of GP-zones (intra-granular precipitates) is similar in un-deformed and deformed alloys, it is concluded that intra-granular precipitation is driven by the same mechanism in deformed and un-deformed microstructures without specific

contribution of strain induced vacancies or of dislocations. A high dislocation density has been however measured by KAM and these defects are known to significantly accelerate precipitation in 7xxx series aluminum alloys [24,44,70]. Most likely, these dislocations are organized in low-angle grain boundaries as suggested by the highly localized KAM contrast observed in Figure 7.

Beyond GP zones, a second population of precipitates nucleated along boundaries has been exhibited by STEM and APT data. Some of them might already exist before artificial aging but solute segregations observed in the as-deformed state should be a transient state that strongly favors such precipitation [71]. In this respect, the deformation-induced segregation would be the key to the observed early development of grain boundary precipitation. Thus, during ageing, grain boundary precipitation develops at the expense of intra-granular precipitation, leading to PFZ. The size of heterogeneously nucleated precipitates is similar in the deformed and un-deformed materials (Figure 10). However, the deformed material contains a much higher fraction of grain boundaries, thus the resulting precipitate size distribution is significantly skewed to larger sizes after annealing (Figure 8). Thus, the fact that precipitation occurs much more rapidly in the deformed material and with a bi-modal distribution can be exclusively related to the higher density of grain and sub-grain boundaries, providing favorable heterogeneous nucleation sites, and finally increasing the proportion of larger heterogeneous precipitates.

During annealing, our experimental data revealed also a significant decrease of the grain size. It is attributed to a slight decrease of the dislocation density which is the sign of a partial recrystallization. During this process, moving boundaries, not pinned by precipitates, must act as solute collectors, playing a role in the PFZ development. This role is most likely prominent in the very early stages of the process where it can be expected that most of the dislocations and grain rearrangement takes place. However, it must be also important at higher temperature when GB motion is activated again resulting in grain growth [62]. This could lead to a faster precipitate dissolution, as suggested by our DSC data above 250°C (Figure 4).

Partial recrystallization in the deformed material annealed at 70°C or 100°C is evidenced by a concomitant decrease of the mean grain size and of the slight decrease of the dislocation density (Fig.7). There is a large number of studies that report about dynamic recrystallization during SPD or about rapid grain growth during post SPD heat treatments (see for example [72–75]), but only few describe a recrystallization (or partial recrystallization) process after SPD leading to a grain size reduction [76,77]. Mangler et al.[76] observed a significant grain size reduction from 77 to 35 nm in a severely deformed Fe-Al alloy after annealing at 220°C and 370°C. They concluded that it was mainly the result of the transformation of sub-grain boundaries into high-angle grain boundaries via the absorption of dislocations. In the present study, KAM maps show that the mean dislocation density decreases during annealing but also that their distribution is modified (Figure 7). Grains appear dislocation free and more pronounced dislocation walls are created. These observations suggest a similar recrystallization mechanism, like in the Fe-Al system. The grain size reduction has certainly been also promoted by the reduced mobility of grain boundaries covered by segregation and even precipitates in the as-deformed state (Figure 3), limiting grain growth. Moreover, since heterogeneous precipitation along intra-granular dislocations could not be observed, this suggests that dislocation recovery occurred faster than heterogeneous precipitation and that partial recrystallization occurred in the early stage of annealing. Since the decrease of the dislocation density is relatively modest, it seems to indicate that only partial recrystallization occurred. It means that not all the microstructure recrystallized, but probably only zones where the driving force was higher. However, in contrast to the diminution of

dislocation density, the diminution of the grain size is important. Consequently, the mechanism of recovery is suggested here to occur together with partial recrystallization. These two mechanisms generally occur simultaneously during ageing, and are difficult to separate in such nanoscale microstructure.

Microstructures achieved after deformation followed by annealing at 70°C or 100°C are qualitatively similar, but exhibit a different balance between different microstructural features. The as-deformed state contains a high, homogeneously distributed dislocation density, GP-zones, grain boundary segregations and some precipitates at grain boundaries. After annealing at 70°C, dislocations are arranged in dislocation walls, the mean grain size is reduced, there is a majority of intra-granular GP zones and few larger inter-granular precipitates. After annealing at 100°C aged, intra-granular precipitates are larger and presumably became mostly η', there is also a much higher fraction of precipitates along boundaries, with PFZ in their vicinity. These microstructural evolutions and the comparison with the un-deformed alloy are schematically presented in Figure 13.

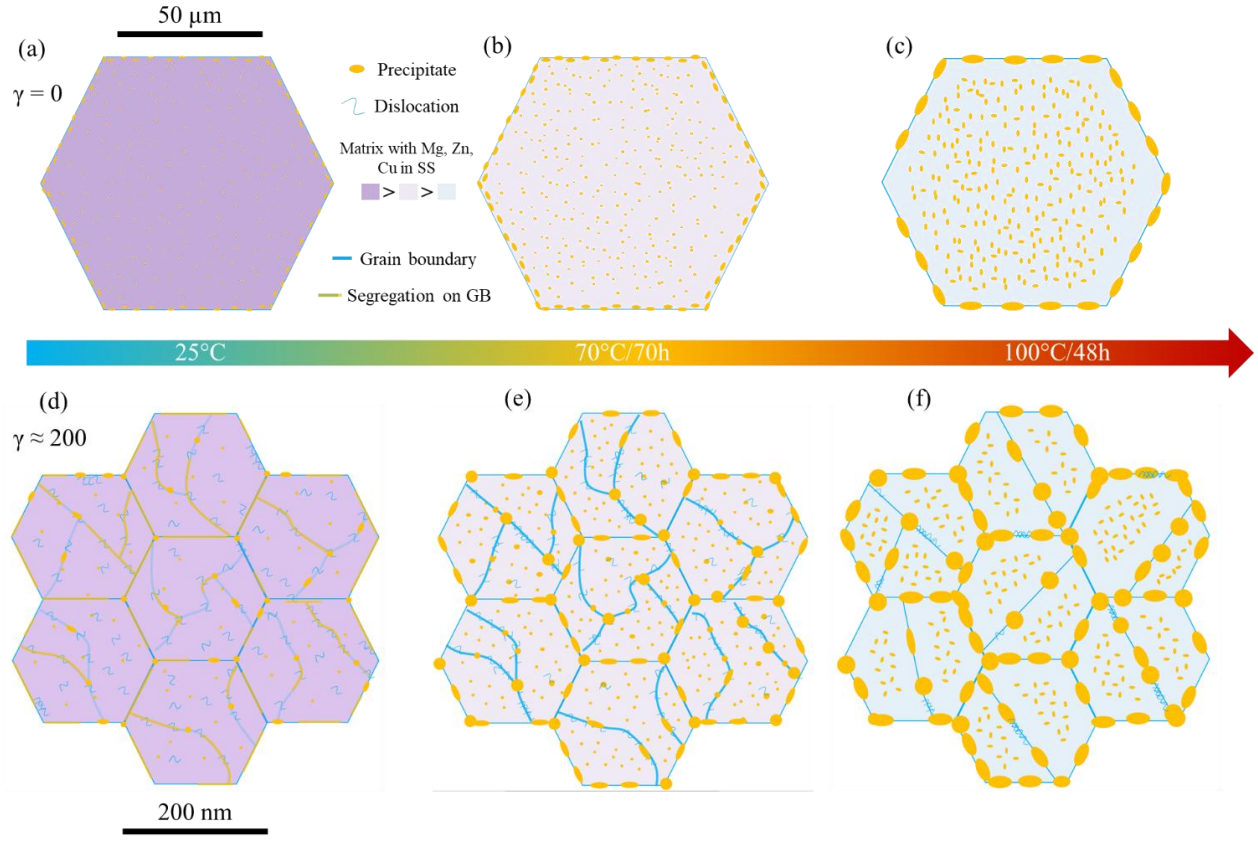

Figure 13: Schematic representation of microstructure evolution for un-deformed (a, b, c) and deformed (d, e, f) at 25°C (a, d), after 70°C/70h (b, e) and after 100°C/48h(c, f).

4.3. Estimated contributions of structural features to the yield stress

To correlate the mechanical behavior to microstructure evolutions, the contribution of each structural features to the yield stress has been estimated.

The grain boundary contribution (σ_{GB}) can be estimated using the Hall-Petch relationship [1,2]. Grains are assumed spherical and their average size is calculated from the grain size distribution weighted by grains surface area (Figure 7):

$$\sigma_{GB} = \sigma_0 + \frac{k}{\sqrt{D}} \quad (3)$$

where σ_0 is the crystal lattice friction (taken as 10 MPa for Al), k is a constant (0.13 $MPa.m^{1/2}$ is taken in this study [78]) and D is the mean grain size.

The dislocation density ρ is estimated from eq.(2) using the average KAM angle [52–54,79,80].

Assuming that dislocation are homogeneously distributed, then their contribution to the yield stress (σ_{dis}), may be estimated according to Taylor, Ashby, Bailey and Hirsch as [81–83] :

$$\sigma_{dis} = M_T \alpha_2 \mu b \rho^{\frac{1}{2}} \quad (4)$$

With the Taylor factor M_T = 2 as proposed in previous works on 7xxx series aluminum alloys [84–86], constant α_2 (= 0.27 for fcc metals); shear modulus μ (= 26.9 GPa for Al 7xxx series alloys) and magnitude of the Burgers vector b (= 0.287 nm for Al).

The precipitates contributions for shearable ($\sigma_{P/sh}$) and by-passed precipitates ($\sigma_{P/by}$) might be estimated from radius and fractions measured by SAXS and TEM. Precipitates are assumed to be spherical and homogeneously distributed [87–89] :

$$\sigma_{p/by} = 0.6 M_T \mu b \frac{\sqrt{f_v}}{R} \quad (5)$$

where, f_v the volume fraction of precipitates and R the mean radius of the precipitates.

$$\sigma_{p/sh} = \sqrt{\frac{3}{4\pi\beta}} \frac{k_p^{3/2} M_T \mu}{\sqrt{b}} (f_v R)^{1/2} \quad (6)$$

With β = 0.43 and k_p = 0.07 [86]. Here, it is considered that: i) the barrier force is proportional to the precipitate radius ($F_m = \alpha\, \mu\, R\, b$); ii) the spatial distribution of precipitates is random [86,87,90,91]; iii) the dislocation tension line is about $\frac{1}{2}\mu b^2$. Then, no distinction is made for the strengthening contribution between GP-zones and η' precipitates as long as they remain shearable.

The critical radius, R_c, to switch from shearing ($\sigma_{P/sh}$) to by-passing ($\sigma_{P/by}$) the precipitates is estimated as $R_c = 0.9\frac{b}{\alpha_3}$ (with α_3 a numerical constant representing the barrier force, $\alpha_3 \approx \frac{1}{10}$ [92]). This gives $R_c \approx 2nm$, thus the precipitation contribution is calculated using eq. (6) if the average radius is below 2nm and using eq. (5) if it is larger than 2nm.

The solid solution contribution (σ_{SS}) was estimated using matrix composition measurements provided by APT analyses and the following equation [86,93,94] :

$$\sigma_{SS} = \sum_i K_i \,.\, C_i^{2/3} \quad (7)$$

where C_i is the concentration of element i in the alloy in wt%, and K_i is a hardening constant related to element i. This constant is defined as K_{Mg}=20.481 MPa.wt%$^{2/3}$, K_{Zn}=3.085 MPa.wt%$^{2/3}$ and K_{Cu}=12.431 MPa.wt%$^{2/3}$ for magnesium, zinc and copper in 7xxx alloys by Dixit, Mishra and Shankaran [95].

Finally, following the approach of Deschamps et al, a non-linear addition of these contributions was applied [86]:

$$\sigma_{tot} = \sigma_{GB} + \sigma_{SS} + \sqrt{{\sigma_{dis}}^2 + (\sigma_{P/sh} + \sigma_{P/by})^2} \quad (8)$$

Experimental parameters used are listed in Table. 4. There is no ambiguity for grain sizes, dislocation densities and solid solution concentrations, but since precipitates have been characterized using several methods, the most reliable and representative data should be selected. SAXS data have intrinsically a much better representativity and statistic as compared to APT and TEM methods. TEM data were used anyway for the deformed material annealed 100°C/48h because SAXS could not measure objects >10nm, while TEM observations demonstrated that at in this state such large particles are abundant.

Experimental		TEM (ASTAR)		APT			SAXS (+TEM)			
		Grain (nm)	**ρ_{dislo} ($.10^{15}$ m^{-2})**	**Mg in SS (wt.%)**	**Zn in SS (wt.%)**	**Cu in SS (wt.%)**	**Intra-granular precipitates**		**Inter-granular precipitates**	
							Radius (nm)	**Volume Fraction**	**Radius (nm)**	**Volume Fraction**
Un-deformed	γ = 0	105000 ± 66000	-	1.6±0.5	8.0±1.3	2.1 ±0.6	0.9±0.3	0.016	4.5±4	<0.00001
	γ = 0 +70°C/70h	105000 ± 66000	-	-	-	-	1.1±0.5	0.066	6.9±3	0.0010
	γ = 0 +100°C/48h	105000 ± 66000	-	-	-	-	1.7±1.2	0.040	4.8±1	0.0002
HPT	γ ≈ 200	213 ± 51	4.2 ± 2.1	1.7±0.2	7.1±1.3	1.9±0.6	0.74±0.3	0.010	3.4±0.8	0.0004
	γ ≈ 200 +70°C/70h	150 ± 15	2.8 ± 1.3	1.3±0.7	5.9±1.3	2.2±0.3	0.83±0.4	0.040	6.8±6.4	0.0150
	γ ≈ 200 +100°C/48h	167 ± 30	2.8 ± 0.7	1.0±0.1	4.4±1.3	2.5±0.4	1.6±1.0	0.010	8.2±3	0.0310

Table. 4 : Summary of experimental measurements, ρ_{dislo} is the dislocation density and SS is the solid solution.

All yield stress contributions that were estimated are listed in Table. 5 and compared to experimental data in Figure 14.

For the un-deformed alloy, the mean grain size is well above one micrometer, thus the grain boundaries contribution is relatively small. Then, the yield stress is mainly governed by the GP-zones and by the solid solution. The calculated yield strength is in good agreement with experimental data (261 ± 18 against 244 ± 52 MPa). After annealing at 70°C, the contribution of shearable precipitates increases significantly. The estimated yield stress is higher than the experimental value. As discussed in section 3.2, this discrepancy could come from different

natural aging or ageing conditions, however this behavior is complicated to understand and need certainly more investigation in the future. After annealing at 100°C, the contribution of shearable and by-passed precipitates is relatively stable and the total estimate is close to the experimental value.

In the deformed material, grain boundaries and dislocations contributions are predominant. The shearable precipitates contribution is less than in the un-deformed alloy since the measured volume fraction of GP-zones was lower. However, the higher fraction of inter-granular precipitates also provides a significant contribution to the yield stress and again our total estimate is in good agreement with experimental data.

The deformed alloy treated at 70°C/70 h exhibits a slight grain size reduction due to partial recrystallization, leading to an increase of the grain boundary contribution. In addition, the contribution of dislocations remains relatively important, while that of GP-zones remains stable whereas the contribution of η'/η precipitates increases. All these contributions allow to reach a yield stress limit close to the measured one.

Last, for the deformed alloy heat treated at 100°C/48 h, grain boundaries, dislocations (including intra-granular disorientation contribution) are still relatively high, and the addition of the precipitate contribution gives a yield stress close to the experimental value.

		σ_{GB}	σ_{dis}	$\sigma_{p/sh}$	$\sigma_{p/by}$	σ_{SS}	σ_{tot}	$\sigma_{experimental}$
Un-deformed γ = 0	25°C	15±5	-	166 ± 13	9 ± 2	61	261 ± 18	244 ± 52
	70°C-70h	15±5	-	374 ± 24	50 ± 10	55	505 ± 42	334
	100°C-48h	15±5	-	362 ± 15	43 ± 6	50	470 ± 13	440
Deformed γ ≈ 200	25°C	260±70	399±107	100 ± 10	69 ± 29	59	673 ± 110	770 ± 23
	70°C-70h	337±17	328±78	253± 22	198 ± 41	50	905 ± 20	849 ± 50
	100°C-48h	320±30	332±42	176 ± 8	235 ± 41	51	847 ± 102	800 ± 22

Table. 5 : Calculated contributions to yield strength compared to the experimental one for the different states. σ_{GB} is the grain boundaries contribution, σ_{dis} the dislocations one, $\sigma_{p/sh}$ and $\sigma_{p/by}$ are for the precipitates contributions, from shearable and by-passed one respectively, σ_{SS} for the solid solution and finally σ_{tot} is the total calculated yield strength and $\sigma_{experimental}$ the experimental one.

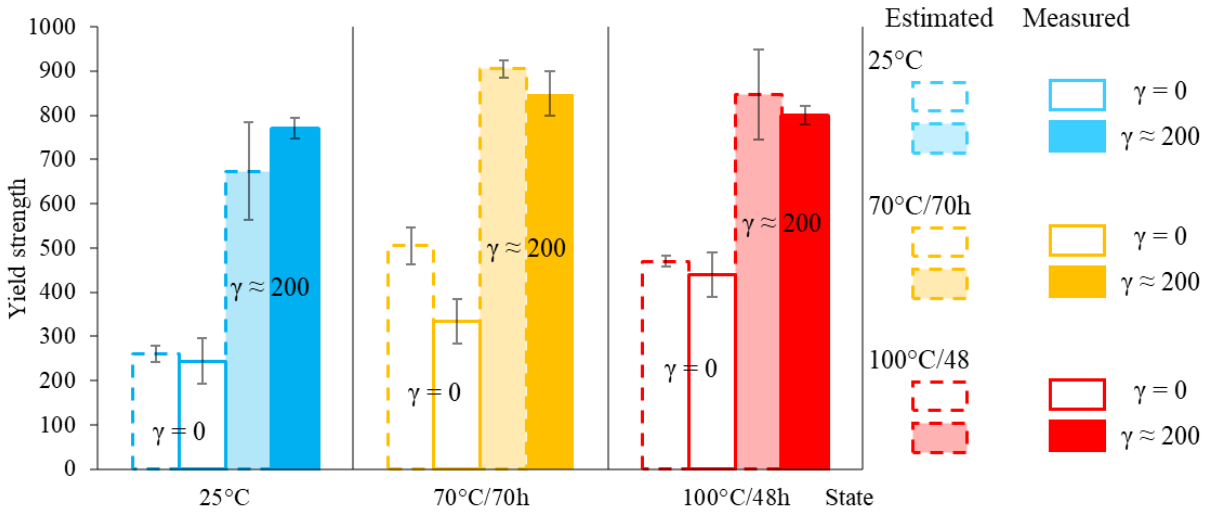

Figure 14 : Comparison between estimated yield strength and measured one for un-deformed and deformed alloys, before and after ageing treatments.

Of course, the agreement between calculated and experimental yield strengths should not be seen as fully predictive, since the model used still has a number of shortcomings with respect to the complexity of the microstructure, among which we can cite: -i- the fact that inter-granular precipitates are obviously located on the grain boundaries probably should change the addition law between these two contributions to yield strength; -ii- adding the contribution of shearable and non-shearable precipitates assumes that they are situated together on the dislocation slip plane, however this is not the case, the two precipitate distributions are located in different parts of the microstructure; -iii- we do not take into account the presence of precipitate-free zones of relatively high fraction, which may influence the early plastic deformation; -iv- the dislocation density contribution is calculated assuming individual dislocations, although in the aged samples dislocations are mainly present as dislocation walls; -iv- the contribution of segregation in deformed state is not take into account.

Indeed, these segregations may have an influence on mechanical properties. Abramova et al. [68] showed an increase of yield strength due to Mo–Cr–Si rich grain boundary segregations in an austenitic stainless steel. This was also proposed in Al-Mg [37,96], in Al-Mg-Cu [69] and in a 7xxx series aluminum alloy [39]. On the contrary, with the presence of Zn at GBs, the strength of an UFG Al-30%Zn alloy reduced considerably due to activation of GB sliding and superplasticity [97]. In the present case there is no evidence of GB sliding or superplasticity on mechanical behavior but if these segregations have a real influence on yield strength, this means that some of the other calculated contributions are overestimated, since the calculated strength is close to the experimental one without taking them into account. In the absence of a clear evidence, we will therefore consider that these segregations have no significant direct influence on the strength of the as-deformed microstructure. Their influence may however be important when considering the grain size reached and the presence of precipitates at structural defects in this very early stage of (natural) ageing.

During ageing of the as-deformed state at the relatively low temperatures studied in the present work (70 and 100°C), the yield stress significantly increases. The evaluation of the different strength contributions allows to understand that this increase comes from the combination of different phenomena. The grain size contribution increases due to the partial recrystallization,

while the dislocation contribution decreases. Interestingly, the addition of these two contributions remains relatively constant. Thus, the relatively strong increase of the yield stress after 70°C ageing is mostly related to the precipitate contributions. There is a high contribution of by-passed precipitates which are mostly located at boundary (heterogeneously nucleated unlike GP zones). Thus, even if they are not located in the grain interiors they seem to significantly affect dislocation motion or nucleation. It further highlights the importance, in such severely plastically deformed alloys, of developing several scales of obstacles to dislocation motion, taking advantage of the different regions of the microstructure (intra and inter-granular), which has been called "hierarchically organized microstructure" in the literature [17]. After 100°C ageing, the situation is similar, with a lower contribution of the intra-granular precipitates which have coarsened, not fully compensated by the increase of the inter-granular precipitates' contribution, due to their coarsening.

The plastic behavior following the yield strength is also of interest. In the three ageing states after deformation, the yield strength is followed by a stage of very high strain hardening ($d\sigma/d\varepsilon$=6000 to 8000 MPa), whose magnitude is larger than that corresponding to the accumulation of internal stress by a full fraction of non-shearable precipitates in these alloys [98], although in the present case only a fraction of the precipitates is expected to be non-shearable. One possible explanation of this behavior for the 100°C aged sample is the presence of comparatively softer precipitate free zones which could trigger plastic deformation at a lower stress than their surroundings. For the other materials this may be related to a composite effect between softer and harder zones of the microstructure due to difference in gran size or precipitate microstructures, when compared to the more homogeneous un-deformed microstructure. The common feature of the three states investigated is the early saturation of engineering stress, and corresponding large proportion of the stress-strain curve following this saturation, and thus in the necking regime. This necking regime is particularly extended in the 100°C aged sample, which confers to this material a higher ductility as compared to the 70°C aged material. On the basis of our microstructural observations, this more extended post-uniform elongation is likely also related to the extensive soft precipitate-free zones, which can accommodate the plastic deformation in the late stages of deformation. The as-deformed material shows a slightly lower strain hardening rate along with a lower yield strength, which allows a larger uniform elongation before Considère's criterion is met. Thus, despite a shorter post-uniform elongation, it shows an elongation to failure comparable with that of the 100°C aged sample. It should be emphasized here that the tensile tests were realized on miniaturized samples of short gauge length, so that the contribution of post-uniform elongation to the total elongation to failure is magnified as compared to more standard tensile specimens. This apparent overestimation must be particularly important in the aged materials that show a small uniform elongation and extended post-uniform elongation.

4. Conclusions

In conclusion, complex interactions between precipitation, grain growth and recrystallization were investigated in an Al-Zn-Mg-Cu alloy that was severely deformed by HPT and aged at low temperature (70°C and 100°C). A combination of submicrometer grain size with nanoscaled precipitates was achieved leading to a yield stress up to 850MPa and to a tensile strength up to 950 MPa. Complementary characterization techniques, such as TEM-ACOM, STEM-HAADF,

APT and SAXS allowed a deep understanding of competing mechanisms leading to structural evolutions during aging and to link final microstructures to the mechanical behavior. The main findings of this study are:

i) During severe plastic deformation, as expected the grain size was reduced in the sub-micrometer range while the dislocation density dramatically increased. Moreover, significant solute segregation (Zn, Cu, Mg) was exhibited at GBs but also along all sub-boundaries. Beyond typical clustering that occurred during natural aging, locally some strain induced heterogeneous precipitation was also revealed. These specific microstructural features lead to a yield stress higher than that achieved after precipitation treatment of the coarse-grained material.

ii) The precipitation kinetic is much faster in the severely deformed alloy and it is also shifted to lower temperatures. During low temperature ageing (70 or 100°C), a significant decrease of the grain size was observed due to partial recrystallization. Precipitates that have heterogeneously precipitated at boundaries act as pinning sites, they reduce their mobility and prevent grain growth. At the same time, the meta-stable solid solution decomposes leading to both intra and inter granular precipitation: η precipitates nucleate on crystalline defects (boundaries and dislocations), GP-zones nucleate in grain interiors and precipitate free zones develop along all boundaries. These microstructural evolutions lead to a significant additional increase the yield stress, mainly attributed to precipitate hardening.

iii)The competition between precipitation/recrystallization/recovery is strongly affected by strain induced segregations and heterogeneous precipitation that pin crystalline defects. Of course, it affects the tensile behavior but some aging conditions could be found where precipitate hardening combine efficiently with grain boundary strengthening (Hall Petch). Due to the fast precipitation kinetic in the deformed structure, such aging treatment must be carried out at reduced temperature as compared to classical precipitation treatments. At 70 or 100°C, it has been possible to promote recrystallization, to limit grain growth and most important to achieve a good balance between homogeneous precipitation (necessary for hardening) and heterogeneous precipitation (necessary to limit grain growth).

Acknowledgments

Both the Agence Nationale de la Recherche (ANR) and the joint CNRS-JSPS 2017 summer program for the support to the trans-national collaboration are gratefully acknowledged for financial support (PRASA project - ANR-15-CE08-0029). This work was also supported in part by Grant-in-Aids for Scientific Research (S) and (A) from the MEXT, Japan (No. JP26220909 and JP19H00830). HPT was carried out in the International Research Center on Giant Straining for Advanced Materials (IRC-GSAM) at Kyushu University. This research has benefited from characterization equipments of the Grenoble INP - CMTC platform supported by the Centre of

Excellence of Multifunctional Architectured Materials "CEMAM" n°ANR-10-LABX-44-01 funded by the Investments for the Future programme.

Bibliography

[1] E.O. Hall, The Deformation and ageing of Mild Steel: III Discussion of Results, Proc. Phys. Soc. B. 64 (1951) 747. https://doi.org/10.1088/0370-1301/64/9/303.

[2] N.J. Petch, The Cleavage Strength of Polycrystals, Journal of the Iron and Steel Institute. 174 (1953) 25–28.

[3] Z.C. Duan, X.Z. Liao, M. Kawasaki, R.B. Figueiredo, T.G. Langdon, Influence of high-pressure torsion on microstructural evolution in an Al–Zn–Mg–Cu alloy, J Mater Sci. 45 (2010) 4621–4630. https://doi.org/10.1007/s10853-010-4400-0.

[4] K.S. Ghosh, N. Gao, M.J. Starink, Characterisation of high pressure torsion processed 7150 Al–Zn–Mg–Cu alloy, Materials Science and Engineering: A. 552 (2012) 164–171. https://doi.org/10.1016/j.msea.2012.05.026.

[5] J. Gubicza, I. Schiller, N.Q. Chinh, J. Illy, Z. Horita, T.G. Langdon, The effect of severe plastic deformation on precipitation in supersaturated Al–Zn–Mg alloys, Materials Science and Engineering: A. 460–461 (2007) 77–85. https://doi.org/10.1016/j.msea.2007.01.001.

[6] Z. Horita, K. Ohashi, T. Fujita, K. Kaneko, T.G. Langdon, Achieving High Strength and High Ductility in Precipitation-Hardened Alloys, Adv. Mater. 17 (2005) 1599–1602. https://doi.org/10.1002/adma.200500069.

[7] M. Cabibbo, E. Evangelista, M. Vedani, Influence of severe plastic deformations on secondary phase precipitation in a 6082 Al-Mg-Si alloy, Metall and Mat Trans A. 36 (2005) 1353–1364. https://doi.org/10.1007/s11661-005-0226-9.

[8] K.R. Cardoso, D.N. Travessa, W.J. Botta, A.M. Jorge, High Strength AA7050 Al alloy processed by ECAP: Microstructure and mechanical properties, Materials Science and Engineering: A. 528 (2011) 5804–5811. https://doi.org/10.1016/j.msea.2011.04.007.

[9] C.M. Cepeda-Jiménez, J.M. García-Infanta, A.P. Zhilyaev, O.A. Ruano, F. Carreño, Influence of the thermal treatment on the deformation-induced precipitation of a hypoeutectic Al–7wt% Si casting alloy deformed by high-pressure torsion, Journal of Alloys and Compounds. 509 (2011) 636–643. https://doi.org/10.1016/j.jallcom.2010.09.122.

[10] M. Murayama, Z. Horita, K. Hono, Microstructure of two-phase Al–1.7 at% Cu alloy deformed by equal-channel angular pressing, Acta Materialia. 49 (2001) 21–29. https://doi.org/10.1016/S1359-6454(00)00308-6.

[11] G. Sha, Y.B. Wang, X.Z. Liao, Z.C. Duan, S.P. Ringer, T.G. Langdon, Influence of equal-channel angular pressing on precipitation in an Al–Zn–Mg–Cu alloy, Acta Materialia. 57 (2009) 3123–3132. https://doi.org/10.1016/j.actamat.2009.03.017.

[12] C. Xu, M. Furukawa, Z. Horita, T.G. Langdon, Using ECAP to achieve grain refinement, precipitate fragmentation and high strain rate superplasticity in a spray-cast aluminum alloy, Acta Materialia. 51 (2003) 6139–6149. https://doi.org/10.1016/S1359-6454(03)00433-6.

[13] J. Zhang, N. Gao, M.J. Starink, Al–Mg–Cu based alloys and pure Al processed by high pressure torsion: The influence of alloying additions on strengthening, Materials Science and Engineering: A. 527 (2010) 3472–3479. https://doi.org/10.1016/j.msea.2010.02.016.

[14] Y.H. Zhao, X.Z. Liao, S. Cheng, E. Ma, Y.T. Zhu, Simultaneously Increasing the Ductility and Strength of Nanostructured Alloys, Advanced Materials. 18 (2006) 2280–2283. https://doi.org/10.1002/adma.200600310.

[15] Y.H. Zhao, X.Z. Liao, Z. Jin, R.Z. Valiev, Y.T. Zhu, Microstructures and mechanical properties of ultrafine grained 7075 Al alloy processed by ECAP and their evolutions

during annealing, Acta Materialia. 52 (2004) 4589–4599. https://doi.org/10.1016/j.actamat.2004.06.017.
[16] B.B. Straumal, B. Baretzky, A.A. Mazilkin, F. Phillipp, O.A. Kogtenkova, M.N. Volkov, R.Z. Valiev, Formation of nanograined structure and decomposition of supersaturated solid solution during high pressure torsion of Al–Zn and Al–Mg alloys, Acta Materialia. 52 (2004) 4469–4478. https://doi.org/10.1016/j.actamat.2004.06.006.
[17] P.V. Liddicoat, X.-Z. Liao, Y. Zhao, Y. Zhu, M.Y. Murashkin, E.J. Lavernia, R.Z. Valiev, S.P. Ringer, Nanostructural hierarchy increases the strength of aluminium alloys, Nature Communications. 1 (2010) 63. https://doi.org/10.1038/ncomms1062.
[18] Z. Feng, X. Luo, Y. Chen, N. Chen, L. Zhang, G. Wu, X. Huang, Effects of precipitates versus solute atoms on the deformation-induced grain refinement in an Al–Cu–Mg alloy, Materials Science and Engineering: A. 771 (2020) 138486. https://doi.org/10.1016/j.msea.2019.138486.
[19] A. Deschamps, F. De Geuser, Z. Horita, S. Lee, G. Renou, Precipitation kinetics in a severely plastically deformed 7075 aluminium alloy, Acta Materialia. 66 (2014) 105–117. https://doi.org/10.1016/j.actamat.2013.11.071.
[20] M.A. Afifi, P.H.R. Pereira, Y.C. Wang, Y. Wang, S. Li, T.G. Langdon, Effect of ECAP processing on microstructure evolution and dynamic compressive behavior at different temperatures in an Al-Zn-Mg alloy, Materials Science and Engineering: A. 684 (2017) 617–625. https://doi.org/10.1016/j.msea.2016.12.099.
[21] S. Sabbaghianrad, T.G. Langdon, A critical evaluation of the processing of an aluminum 7075 alloy using a combination of ECAP and HPT, Materials Science and Engineering: A. 596 (2014) 52–58. https://doi.org/10.1016/j.msea.2013.12.034.
[22] G. Nurislamova, X. Sauvage, M. Murashkin, R. Islamgaliev, R. Valiev, Nanostructure and related mechanical properties of an Al–Mg–Si alloy processed by severe plastic deformation, Philosophical Magazine Letters. 88 (2008) 459–466. https://doi.org/10.1080/09500830802186938.
[23] H. Queudet, S. Lemonnier, E. Barraud, J. Guyon, J. Ghanbaja, N. Allain, E. Gaffet, One-step consolidation and precipitation hardening of an ultrafine-grained Al-Zn-Mg alloy powder by Spark Plasma Sintering, Materials Science and Engineering: A. 685 (2017) 227–234. https://doi.org/10.1016/j.msea.2017.01.009.
[24] K. Ma, T. Hu, H. Yang, T. Topping, A. Yousefiani, E.J. Lavernia, J.M. Schoenung, Coupling of dislocations and precipitates: Impact on the mechanical behavior of ultrafine grained Al–Zn–Mg alloys, Acta Materialia. 103 (2016) 153–164. https://doi.org/10.1016/j.actamat.2015.09.017.
[25] M.V. Markushev, E.V. Avtokratova, S.V. Krymskiy, O.Sh. Sitdikov, Effect of precipitates on nanostructuring and strengthening of high-strength aluminum alloys under high pressure torsion, Journal of Alloys and Compounds. 743 (2018) 773–779. https://doi.org/10.1016/j.jallcom.2018.02.047.
[26] A. Duchaussoy, X. Sauvage, K. Edalati, Z. Horita, G. Renou, A. Deschamps, F. De Geuser, Structure and mechanical behavior of ultrafine-grained aluminum-iron alloy stabilized by nanoscaled intermetallic particles, Acta Materialia. 167 (2019) 89–102. https://doi.org/10.1016/j.actamat.2019.01.027.
[27] R.Z. Valiev, Yu.V. Ivanisenko, E.F. Rauch, B. Baudelet, Structure and deformation behaviour of Armco iron subjected to severe plastic deformation, Acta Materialia. 44 (1996) 4705–4712. https://doi.org/10.1016/S1359-6454(96)00156-5.

[28] Y. Ito, Z. Horita, Microstructural evolution in pure aluminum processed by high-pressure torsion, Materials Science and Engineering: A. 503 (2009) 32–36. https://doi.org/10.1016/j.msea.2008.03.055.
[29] J. Jiang, Y. Ding, F. Zuo, A. Shan, Mechanical properties and microstructures of ultrafine-grained pure aluminum by asymmetric rolling, Scripta Materialia. 60 (2009) 905–908. https://doi.org/10.1016/j.scriptamat.2009.02.016.
[30] M. Kawasaki, Z. Horita, T.G. Langdon, Microstructural evolution in high purity aluminum processed by ECAP, Materials Science and Engineering: A. 524 (2009) 143–150. https://doi.org/10.1016/j.msea.2009.06.032.
[31] V.V. Stolyarov, V.V. Latysh, V.A. Shundalov, D.A. Salimonenko, R.K. Islamgaliev, R.Z. Valiev, Influence of severe plastic deformation on aging effect of Al-Zn-Mg-Cu-Zr alloy, Materials Science and Engineering: A. 234–236 (1997) 339–342. https://doi.org/10.1016/S0921-5093(97)00210-4.
[32] R.K. Islamgaliev, N.F. Yunusova, I.N. Sabirov, A.V. Sergueeva, R.Z. Valiev, Deformation behavior of nanostructured aluminum alloy processed by severe plastic deformation, Materials Science and Engineering: A. 319–321 (2001) 877–881. https://doi.org/10.1016/S0921-5093(01)01052-8.
[33] Y. Zhang, S. Jin, P. Trimby, X. Liao, M.Y. Murashkin, R.Z. Valiev, G. Sha, Strengthening mechanisms in an ultrafine-grained AlZnMgCu alloy processed by high pressure torsion at different temperatures, Materials Science and Engineering: A. 752 (2019) 223–232. https://doi.org/10.1016/j.msea.2019.02.094.
[34] M. Borodachenkova, F. Barlat, W. Wen, A. Bastos, J.J. Grácio, A microstructure-based model for describing the material properties of Al–Zn alloys during high pressure torsion, International Journal of Plasticity. 68 (2015) 150–163. https://doi.org/10.1016/j.ijplas.2014.01.009.
[35] Y. Ito, K. Edalati, Z. Horita, High-pressure torsion of aluminum with ultrahigh purity (99.9999%) and occurrence of inverse Hall-Petch relationship, Materials Science and Engineering: A. 679 (2017) 428–434. https://doi.org/10.1016/j.msea.2016.10.066.
[36] X. Sauvage, A. Duchaussoy, G. Zaher, Strain Induced Segregations in Severely Deformed Materials, Materials Transactions. 60 (2019) 1151–1158. https://doi.org/10.2320/matertrans.MF201919.
[37] X. Sauvage, N. Enikeev, R. Valiev, Y. Nasedkina, M. Murashkin, Atomic-scale analysis of the segregation and precipitation mechanisms in a severely deformed Al–Mg alloy, Acta Materialia. 72 (2014) 125–136. https://doi.org/10.1016/j.actamat.2014.03.033.
[38] G. Sha, L. Yao, X. Liao, S.P. Ringer, Z. Chao Duan, T.G. Langdon, Segregation of solute elements at grain boundaries in an ultrafine grained Al–Zn–Mg–Cu alloy, Ultramicroscopy. 111 (2011) 500–505. https://doi.org/10.1016/j.ultramic.2010.11.013.
[39] Y. Zhang, S. Jin, P.W. Trimby, X. Liao, M.Y. Murashkin, R.Z. Valiev, J. Liu, J.M. Cairney, S.P. Ringer, G. Sha, Dynamic precipitation, segregation and strengthening of an Al-Zn-Mg-Cu alloy (AA7075) processed by high-pressure torsion, Acta Materialia. 162 (2019) 19–32. https://doi.org/10.1016/j.actamat.2018.09.060.
[40] X. Sauvage, E.V. Bobruk, M.Yu. Murashkin, Y. Nasedkina, N.A. Enikeev, R.Z. Valiev, Optimization of electrical conductivity and strength combination by structure design at the nanoscale in Al–Mg–Si alloys, Acta Materialia. 98 (2015) 355–366. https://doi.org/10.1016/j.actamat.2015.07.039.
[41] Y. Nasedkina, X. Sauvage, E.V. Bobruk, M.Yu. Murashkin, R.Z. Valiev, N.A. Enikeev, Mechanisms of precipitation induced by large strains in the Al-Cu system, Journal of

Alloys and Compounds. 710 (2017) 736–747. https://doi.org/10.1016/j.jallcom.2017.03.312.
[42] A. Deschamps, F. Livet, Y. Bréchet, Influence of predeformation on ageing in an Al–Zn–Mg alloy—I. Microstructure evolution and mechanical properties, Acta Materialia. 47 (1998) 281–292. https://doi.org/10.1016/S1359-6454(98)00293-6.
[43] A. Deschamps, G. Fribourg, Y. Bréchet, J.L. Chemin, C.R. Hutchinson, In situ evaluation of dynamic precipitation during plastic straining of an Al–Zn–Mg–Cu alloy, Acta Materialia. 60 (2012) 1905–1916. https://doi.org/10.1016/j.actamat.2012.01.002.
[44] S.-S. Wang, J.-T. Jiang, G.-H. Fan, A.M. Panindre, G.S. Frankel, L. Zhen, Accelerated precipitation and growth of phases in an Al-Zn-Mg-Cu alloy processed by surface abrasion, Acta Materialia. 131 (2017) 233–245. https://doi.org/10.1016/j.actamat.2017.03.074.
[45] N. Gao, M.J. Starink, M. Furukawa, Z. Horita, C. Xu, T.G. Langdon, Evolution of Microstructure and Precipitation in Heat-Treatable Aluminium Alloys during ECA Pressing and Subsequent Heat Treatment, Materials Science Forum. 503–504 (2006) 275–280. https://doi.org/10.4028/www.scientific.net/MSF.503-504.275.
[46] Y. Huang, J.D. Robson, P.B. Prangnell, The formation of nanograin structures and accelerated room-temperature theta precipitation in a severely deformed Al–4wt.% Cu alloy, Acta Materialia. 58 (2010) 1643–1657. https://doi.org/10.1016/j.actamat.2009.11.008.
[47] K. Edalati, Z. Horita, A review on high-pressure torsion (HPT) from 1935 to 1988, Materials Science and Engineering: A. 652 (2016) 325–352. https://doi.org/10.1016/j.msea.2015.11.074.
[48] E. Rauch, M. Véron, Automated crystal orientation and phase mapping in TEM, Materials Characterization. 98 (2014) 1–9. https://doi.org/10.1016/j.matchar.2014.08.010.
[49] E. Rauch, M. Véron, S. Nicolopoulos, D. Bultreys, Orientation and Phase Mapping in TEM Microscopy (EBSD-TEM Like): Applications to Materials Science, Solid State Phenomena. 186 (2012) 13–15. https://doi.org/10.4028/www.scientific.net/SSP.186.13.
[50] D. Viladot, M. Véron, M. Gemmi, F. Peiró, J. Portillo, S. Estradé, J. Mendoza, N. Llorca- Isern, S. Nicolopoulos, Orientation and phase mapping in the transmission electron microscope using precession-assisted diffraction spot recognition: state-of-the-art results, Journal of Microscopy. 252 (2013) 23–34. https://doi.org/10.1111/jmi.12065.
[51] E. Rauch, S. Rouvimov, S. Nicolopoulos, P. Moeck, High Throughput Automated Crystal Orientation and Phase Mapping of Nanoparticles from HREM - TEM Images, Microscopy and Microanalysis. 15 (2009) 756–757. https://doi.org/10.1017/S1431927609099607.
[52] M. Calcagnotto, D. Ponge, E. Demir, D. Raabe, Orientation gradients and geometrically necessary dislocations in ultrafine grained dual-phase steels studied by 2D and 3D EBSD, Materials Science and Engineering: A. 527 (2010) 2738–2746. https://doi.org/10.1016/j.msea.2010.01.004.
[53] Q. Liu, D. Juul Jensen, N. Hansen, Effect of grain orientation on deformation structure in cold-rolled polycrystalline aluminium, Acta Materialia. 46 (1998) 5819–5838. https://doi.org/10.1016/S1359-6454(98)00229-8.
[54] Y. Takayama, J.A. Szpunar, H. Kato, Analysis of Intragranular Misorientation Related to Deformation in an Al-Mg-Mn Alloy, Materials Science Forum. (2005). https://doi.org/10.4028/www.scientific.net/MSF.495-497.1049.

[55] A. Kumar, G. Agarwal, R. Petrov, S. Goto, J. Sietsma, M. Herbig, Microstructural evolution of white and brown etching layers in pearlitic rail steels, Acta Materialia. 171 (2019) 48–64. https://doi.org/10.1016/j.actamat.2019.04.012.
[56] I. Bressler, B.R. Pauw, A.F. Thünemann, McSAS: software for the retrieval of model parameter distributions from scattering patterns, J Appl Cryst. 48 (2015) 962–969. https://doi.org/10.1107/S1600576715007347.
[57] B.R. Pauw, J.S. Pedersen, S. Tardif, M. Takata, B.B. Iversen, Improvements and considerations for size distribution retrieval from small-angle scattering data by Monte Carlo methods, J Appl Cryst. 46 (2013) 365–371. https://doi.org/10.1107/S0021889813001295.
[58] J. Hyde, G. Da Costa, C. Hatzoglou, H. Weekes, B. Radiguet, P. Styman, F. Vurpillot, C. Pareige, A. Etienne, G. Bonny, N. Castin, L. Malerba, P. Pareige, Analysis of Radiation Damage in Light Water Reactors: Comparison of Cluster Analysis Methods for the Analysis of Atom Probe Data, Microscopy and Microanalysis. 23 (2017) 366–375. https://doi.org/10.1017/s1431927616012678.
[59] C. Schmuck, P. Auger, F. Danoix, D. Blavette, Quantitative analysis of GP zones formed at room temperature in a 7150 Al-based alloy, Applied Surface Science. 87–88 (1995) 228–233. https://doi.org/10.1016/0169-4332(94)00501-X.
[60] S.K. Maloney, K. Hono, I.J. Polmear, S.P. Ringer, The chemistry of precipitates in an aged Al-2.1Zn-1.7Mg at.% alloy, Scripta Materialia. 41 (1999) 1031–1038. https://doi.org/10.1016/S1359-6462(99)00253-5.
[61] S. Liu, C. Li, S. Han, Y. Deng, X. Zhang, Effect of natural aging on quench-induced inhomogeneity of microstructure and hardness in high strength 7055 aluminum alloy, Journal of Alloys and Compounds. 625 (2015) 34–43. https://doi.org/10.1016/j.jallcom.2014.10.195.
[62] H. Zhao, F. De Geuser, A. Kwiatkowski da Silva, A. Szczepaniak, B. Gault, D. Ponge, D. Raabe, Segregation assisted grain boundary precipitation in a model Al-Zn-Mg-Cu alloy, Acta Materialia. 156 (2018) 318–329. https://doi.org/10.1016/j.actamat.2018.07.003.
[63] J.I. Rojas, D. Crespo, Dynamic microstructural evolution of an Al–Zn–Mg–Cu alloy (7075) during continuous heating and the influence on the viscoelastic response, Materials Characterization. 134 (2017) 319–328. https://doi.org/10.1016/j.matchar.2017.11.018.
[64] N.Q. Chinh, J. Lendvai, D.H. Ping, K. Hono, The effect of Cu on mechanical and precipitation properties of Al–Zn–Mg alloys, Journal of Alloys and Compounds. 378 (2004) 52–60. https://doi.org/10.1016/j.jallcom.2003.11.175.
[65] G. Sha, A. Cerezo, Early-stage precipitation in Al–Zn–Mg–Cu alloy (7050), Acta Materialia. 52 (2004) 4503–4516. https://doi.org/10.1016/j.actamat.2004.06.025.
[66] X. Sauvage, F. Wetscher, P. Pareige, Mechanical alloying of Cu and Fe induced by severe plastic deformation of a Cu–Fe composite, Acta Materialia. 53 (2005) 2127–2135. https://doi.org/10.1016/j.actamat.2005.01.024.
[67] O. Cojocaru-Mirédin, D. Mangelinck, K. Hoummada, E. Cadel, D. Blavette, B. Deconihout, C. Perrin-Pellegrino, Snowplow effect and reactive diffusion in the Pt doped Ni–Si system, Scripta Materialia. 57 (2007) 373–376. https://doi.org/10.1016/j.scriptamat.2007.05.007.
[68] M.M. Abramova, N.A. Enikeev, R.Z. Valiev, A. Etienne, B. Radiguet, Y. Ivanisenko, X. Sauvage, Grain boundary segregation induced strengthening of an ultrafine-grained austenitic stainless steel, Materials Letters. C (2014) 349–352. https://doi.org/10.1016/j.matlet.2014.07.188.

[69] T. Masuda, X. Sauvage, S. Hirosawa, Z. Horita, Achieving highly strengthened Al–Cu–Mg alloy by grain refinement and grain boundary segregation, Materials Science and Engineering: A. 793 (2020) 139668. https://doi.org/10.1016/j.msea.2020.139668.
[70] K. Ma, H. Wen, T. Hu, T.D. Topping, D. Isheim, D.N. Seidman, E.J. Lavernia, J.M. Schoenung, Mechanical behavior and strengthening mechanisms in ultrafine grain precipitation-strengthened aluminum alloy, Acta Materialia. 62 (2014) 141–155. https://doi.org/10.1016/j.actamat.2013.09.042.
[71] H. Zhao, B. Gault, D. Ponge, D. Raabe, F. De Geuser, Parameter free quantitative analysis of atom probe data by correlation functions: Application to the precipitation in Al-Zn-Mg-Cu, Scripta Materialia. 154 (2018) 106–110. https://doi.org/10.1016/j.scriptamat.2018.05.024.
[72] X. Liu, Y. Li, Y. Man, J. Wang, R. Xu, Precipitation and recrystallization of HPT-processed Mg-Sm-Ca alloy at low temperatures, Materials Letters. 277 (2020) 128252. https://doi.org/10.1016/j.matlet.2020.128252.
[73] O.V. Mishin, A. Godfrey, T. Yu, N. Hansen, D.J. Jensen, Evolution of microstructure and texture during recovery and recrystallization in heavily rolled aluminum, IOP Conf. Ser.: Mater. Sci. Eng. 82 (2015) 012083. https://doi.org/10.1088/1757-899X/82/1/012083.
[74] K. Lu, Stabilizing nanostructures in metals using grain and twin boundary architectures, Nature Reviews Materials. 1 (2016) 16019. https://doi.org/10.1038/natrevmats.2016.19.
[75] M. Ames, J. Markmann, R. Karos, A. Michels, A. Tschöpe, R. Birringer, Unraveling the nature of room temperature grain growth in nanocrystalline materials, Acta Materialia. 56 (2008) 4255–4266. https://doi.org/10.1016/j.actamat.2008.04.051.
[76] C. Mangler, C. Gammer, H.P. Karnthaler, C. Rentenberger, Structural modifications during heating of bulk nanocrystalline FeAl produced by high-pressure torsion, Acta Materialia. 58 (2010) 5631–5638. https://doi.org/10.1016/j.actamat.2010.06.036.
[77] C. Gammer, H.P. Karnthaler, C. Rentenberger, Unexpected grain size reduction by heating in bulk nanocrystalline FeAl, Journal of Alloys and Compounds. 633 (2015) 384–389. https://doi.org/10.1016/j.jallcom.2015.01.186.
[78] T. Shanmugasundaram, M. Heilmaier, B.S. Murty, V.S. Sarma, On the Hall–Petch relationship in a nanostructured Al–Cu alloy, Materials Science and Engineering: A. 527 (2010) 7821–7825. https://doi.org/10.1016/j.msea.2010.08.070.
[79] L.P. Kubin, A. Mortensen, Geometrically necessary dislocations and strain-gradient plasticity: a few critical issues, Scripta Materialia. 48 (2003) 119–125. https://doi.org/10.1016/S1359-6462(02)00335-4.
[80] H. Gao, Y. Huang, W.D. Nix, J.W. Hutchinson, Mechanism-based strain gradient plasticity— I. Theory, Journal of the Mechanics and Physics of Solids. 47 (1999) 1239–1263. https://doi.org/10.1016/S0022-5096(98)00103-3.
[81] J.W. Taylor, Dislocation Dynamics and Dynamic Yielding, Journal of Applied Physics. 36 (1965) 3146–3150. https://doi.org/10.1063/1.1702940.
[82] M.F. Ashby, The deformation of plastically non-homogeneous materials, The Philosophical Magazine: A Journal of Theoretical Experimental and Applied Physics. 21 (1970) 399–424. https://doi.org/10.1080/14786437008238426.
[83] J.E. Bailey, P.B. Hirsch, The dislocation distribution, flow stress, and stored energy in cold-worked polycrystalline silver, The Philosophical Magazine: A Journal of Theoretical Experimental and Applied Physics. 5 (1960) 485–497. https://doi.org/10.1080/14786436008238300.

[84] R. Ghiaasiaan, S. Shankar, Structure-property models in Al-Zn-Mg-Cu alloys: A critical experimental assessment of shape castings, Materials Science and Engineering: A. 733 (2018) 235–245. https://doi.org/10.1016/j.msea.2018.07.048.
[85] M.J. Starink, S.C. Wang, A model for the yield strength of overaged Al–Zn–Mg–Cu alloys, Acta Materialia. 51 (2003) 5131–5150. https://doi.org/10.1016/S1359-6454(03)00363-X.
[86] A. Deschamps, Y. Brechet, Influence of predeformation and ageing of an Al–Zn–Mg alloy—II. Modeling of precipitation kinetics and yield stress, Acta Materialia. 47 (1998) 293–305. https://doi.org/10.1016/S1359-6454(98)00296-1.
[87] U.F. Kocks, Statistical treatment of penetrable obstacles, Can. J. Phys. 45 (1967) 737–755. https://doi.org/10.1139/p67-056.
[88] E. Orowan, Discussion on internal stresses. Symposium on Internal Stresses in Metals and Alloys, (1948) 451–453.
[89] U.F. Kocks, A statistical theory of flow stress and work-hardening, The Philosophical Magazine: A Journal of Theoretical Experimental and Applied Physics. 13 (1966) 541–566. https://doi.org/10.1080/14786436608212647.
[90] J. Friedel, Dislocations Pergamon, New York. 274 (1964).
[91] R. Labusch, Die „Aktivierungslänge“ bei der thermischen Versetzungsbewegung über Hindernisse auf der Gleitebene, Z. Physik. 167 (1962) 452–460. https://doi.org/10.1007/BF01378124.
[92] A. Deschamps, Y. Bréchet, F. Livet, Influence of copper addition on precipitation kinetics and hardening in Al–Zn–Mg alloy, Materials Science and Technology. 15 (1999) 993–1000. https://doi.org/10.1179/026708399101506832.
[93] M.J. Starink, N. Gao, L. Davin, J. Yan, A. Cerezo, Room temperature precipitation in quenched Al–Cu–Mg alloys: a model for the reaction kinetics and yield strength development, Philosophical Magazine. 85 (2005) 1395–1417. https://doi.org/10.1080/14786430412331333374.
[94] O. Myhr, Ø. Grong, S. Andersen, Modelling of the age hardening behaviour of Al–Mg–Si alloys, Acta Materialia. 49 (2001) 65–75. https://doi.org/10.1016/S1359-6454(00)00301-3.
[95] M. Dixit, R.S. Mishra, K.K. Sankaran, Structure–property correlations in Al 7050 and Al 7055 high-strength aluminum alloys, Materials Science and Engineering: A. 478 (2008) 163–172. https://doi.org/10.1016/j.msea.2007.05.116.
[96] R.Z. Valiev, N.A. Enikeev, M.Yu. Murashkin, S.E. Aleksandrov, R.V. Goldshtein, Superstrength of ultrafine-grained aluminum alloys produced by severe plastic deformation, Dokl. Phys. 55 (2010) 267–270. https://doi.org/10.1134/S1028335810060054.
[97] K. Edalati, Z. Horita, R.Z. Valiev, Transition from poor ductility to room-temperature superplasticity in a nanostructured aluminum alloy, Scientific Reports. 8 (2018) 1–8. https://doi.org/10.1038/s41598-018-25140-1.
[98] G. Fribourg, Y. Bréchet, A. Deschamps, A. Simar, Microstructure-based modelling of isotropic and kinematic strain hardening in a precipitation-hardened aluminium alloy, Acta Materialia. 59 (2011) 3621–3635. https://doi.org/10.1016/j.actamat.2011.02.035.